Trinity College Dublin
Coláiste na Tríonóide, Baile Átha Cliath
The University of Dublin

Working Principle of Tunable Plasmonic Reflect-Array Metasurfaces

Trinity College Dublin

November 2021

Name: Sara Pelivani

Supervisor: Prof. Louise Bradley

Student No: 15319249

Declaration

I declare that this thesis has not been submitted as an exercise for a degree at this or any other university and it is entirely my own work.

I agree to deposit this thesis in the University's open access institutional repository or allow the library to do so on my behalf, subject to Irish Copyright Legislation and Trinity College Library conditions of use and acknowledgement.

Abstract

This thesis will explore the way in which plasmonic metasurfaces, hosting nano-scale metallic resonator elements, can be used as beam-steering devices. We will propose our own devices that will demonstrate anomalous reflection (at a pre-determined reflection angle), despite being illuminated by normal incident light. The performance of these devices will be investigated in the near-infrared region of the spectrum, though their working principle is not limited to such a narrow wavelength range. Through the incorporation of a phase-change-material, our devices will be able to support dynamic control over the reflected radiation post-fabrication. Different methods of achieving this control over the propagation path of scattered radiation are explored and compared. I.e. anomalous reflection is shown to be realised by varying the geometry of the resonator element along the device surface, varying the local environment surrounding each resonator element, or both of these variations in unison.

All metasurface devices presented in this work will employ a metal-insulator-metal structure. Therefore, our first objective was to optimise the performance of such a device by conducting a comparative study between three difference Drude-like metals (gold, silver, and aluminium). Through this study, the ideal material (and material properties) of the top metallic resonator element and bottom back-reflector could be determined. The ideal resonator element material was found to be gold and silver, while the ideal back-reflector material was found to be aluminium. The performance of a device which employed this combination of materials was presented, exhibiting a maximum anomalous reflection angle of $\sim 40^\circ$ at an incident wavelength of 1550 nm. This device used variations in the geometry of the resonator elements in order to achieve the impressive anomalous reflection.

The performance of an alternative device is also reported. This device utilises variations in the local environment surrounding each resonator element, and is capable of achieving the largest dynamic angle sweep of $\sim 54^\circ$ at an incident wavelength of 1000 nm. A device which employes both of these methods to achieve anomalous reflection is also proposed. Such a device is shown to be able to achieve an anomalous reflection angle of $\sim 33^\circ$ also at an incident wavelength of 1000 nm.

The advantages, disadvantages, and extent to which each device can achieve dynamic control over the reflected radiation post-fabrication is discussed.

Acknowledgments

I would like to start by giving a big thanks to my postgraduate supervisor, Prof. Louise Bradley. Her guidance, support, and encouragement during the course of my Master's programme ensured the smooth running of the project, overcoming the disturbances caused by the COVID pandemic. I would also like to thank the members of the research group, including the summer students who came and went , for their support and friendship. In particular, I would like to thank Calin Hrelescu, and Xia Zhang for showing me how to use the simulation programme necessary for my research. Thanks to Stephen Cunningham for the time he took to train me up on the equipment I would have needed to fabricate my devices, though the original plan to create the devices had to change due to COVID.

List of Figures

List of Tables

Contents

Chapter 1

1 Introduction

1.1 Motivation

The objective of this work is to design and optimise nano-scale devices capable of controlling the direction of scattered radiation. Traditionally the manipulation of electromagnetic radiation has been realised through bulky optical components. These components are capable of gradually modulating the phase of incident radiation, thus allowing for control of the propagation path of the reflected and transmitted light [1]. Inconveniently, achieving a specific phase shift demands the propagation length to be commensurate with the operation wavelength. In order to avoid such bulky structures and manipulate light in a sub-wavelength scale, one must employ a metamaterial. The transition of these optical devices into the nano-scale has expedited its passage into a wide range of scientific disciplines.

A metamaterial is a structure that typically (though not strictly) contains periodically arranged resonators on a dielectric substrate. The elaborate construction of these resonators allows the effective medium to possess certain bulk properties which are not found in conventional materials, but are not forbidden by Maxwell's equations. A metasurface is analogous to a metamaterial, though can be regarded as the two-dimensional equivalent. Throughout the years, metasurfaces have been fabricated in various ways to create a large range of optical devices. These optical devices have the ability to enable control of the phase [2, 3, 4], amplitude [5], and polarisation [6, 7] of impinging electromagnetic radiation. Such devices include dynamic holographic displays [8, 9], on-chip optical devices [10, 11], beam-steering [3, 12], radar scanning systems, LiDAR [13], flat lenses [14, 15], extraordinary optical transmission (EOT) [16], invisibility cloaking [17], imaging applications [18], and much more. One can develop a beam-steering device by creating a metasurface that can successfully govern the angle of reflection or transmittance of scattered radiation. One can go a step further by introducing an active component within the metasurface, allowing for dynamic control of the reflected/transmitted angle.

Though the operation of metasurfaces is comparable to that of conventional optical components, the working principle does not reply on propagation effects. Rather, metasurfaces alter the

direction of propagation of incident light by introducing local phase shifts through sub-wavelength optical resonators [19]. The spacing between these resonators must also be on the sub-wavelength scale, as governed by Huygen's principle [20]. Previous works have reported on the operations of metasurfaces using different types of optical elements, such as dielectric [21], plasmonic [2, 22], and various shaped apertures in metallic films [3, 12]. These devices differ in the way in which their resonator elements alter the phase of the impinging radiation. We will primarily focus on the phase modulation achieved by plasmonic metasurfaces, where a metallic nano-particle will behave as the resonator element. These metallic elements host surface plasmons which can have a strong interaction with impinging radiation in such a way as to detune the element from its resonant frequency (discussed in greater detail in Section 2.1) [23]. Through careful design, one can fabricate a structure in which each consecutive element is further detuned from the resonant frequency. This will generate a spatially varying phase, which can be used to engineer the scattered wavefronts in such a way as to give the desired angle of reflection or transmittance. The relationship between the phase modulation and the scattered angles is described by Snell's Generalised law (see Section 2.2.1) [24].

One can achieve this spatially varying phase shift by either spatially varying the geometry (i.e. width, height, etc.) of the resonator element, or varying the local environment of each element. Adjusting either of these factors leads to the detuning of the elements from the resonant frequency. Alternatively, one can also fabricate a metasurface where the phase response is achieved at the boundary between optically thin, lossy materials. This phase shift can vary between 0 and π [25, 26]. However, if we want full control of the scattered wavefront, we require our metasurface to realise the maximum phase coverage possible, i.e. from 0 to 2π, therefore, this paper will investigate the effects of employing the former two methods.

One drawback of metasurfaces or reflectarrays is that the final emitted wavefront configuration is fixed. A way to overcome this disadvantage is by incorporating a phase-changing material (PCM) into the metasurface structure. PCMs have the ability to change optical (refractive index and extinction coefficient) and electrical (resistivity) properties when heated beyond a transition temperature (T_{MIT}). This will be discussed in greater detail in Section 2.3. Previous studies by Carlota Ruiz *et al.* have reported on the use of $Ge_2Sb_2Te_5$ (GST) as the PCM in their metasurface structure [22, 27]. They took advantage of the phase changing properties of GST to realise

a dynamic beam-steering device. When the GST layer was in its amorphous state (below T_{MIT}), the metasurface was fashioned to reflect light at a predetermined angle under normal incidence conditions. However, when the GST transitioned to its crystalline state, the underlying resonant behaviour of each resonator was cancelled, and ordinary specular reflection was reestablished. Therefore, introducing this PCM enabled the fabrication of a device no longer comprising of exclusively passive components which limits the reflected radiation to a fixed direction. Perhaps a superior PCM is the transition-metal oxide known as vanadium dioxide (VO_2). Similar to GST, VO_2 allows for reversible and ultra-fast phase changes. However, VO_2 exhibits an abrupt change from an insulator (monoclinic phase) to a metal (rutile phase) at a lower temperature (68 °C) [28] relative to GST (between 100°C and 150°C) [29]. This makes VO_2 a more energy-efficient PCM.

PCMs may also be used to modify the local environment of each optical element. For example, if the PCM exhibits a continuous phase change when exposed to a thermal stimulus, one could establish a device which enables control over the temperature of each element, and therefore the optical properties of the PCM. Previous works have reported on the large, continuous phase shifts this approach can achieve when utilising VO_2 within the metasurface [2, 3]. Contrary to the work of Carlota Ruiz *et al.*, these thermal-gradient based metasurfaces can achieve continuous control over the angle of reflection or transmittance, as opposed to discretely switching between specular and anomalous reflection.

1.2 Thesis Outline

The work presented in this thesis is simulation based. However, the devices were designed in such a way as to try and ensure the feasibility of experimental realisation. The performance of the proposed devices was investigated when subject to normal incident radiation in the near-infrared (NIR) region of the spectrum, though the working principle behind these metasurfaces is not limited to such a narrow wavelength range. The design of metasurface devices optimised to the NIR has a large range of applications, including those mentioned in Section 1.1. The potential integration of these metasurface devices operating in the NIR is particularly important for medical diagnostic applications [30, 31]. This is as radiation in the NIR has an acute penetration depth in tissue and cells at the molecular level [32]. The structure of the thesis is outlines below:

- **Chapter 2** provides background information necessary for understanding the working principle behind the proposed metasurface beam-steering devices. Since the devices will host metal resonator elements/wires, it is vital to introduce the concept of surface plasmons (Sections 2.1.1-2.1.4) and explore how their presence affects the local phase response for each resonator (Sections 2.1.5-2.1.7). The relationship between these local phase responses and the direction of scattered radiation is also discussed (Section 2.2). Finally, the phase changing properties of VO_2 is explored, which will be useful in understanding how post-fabrication, dynamic control over the reflected radiation can be realised by our metasurface devices (Section 2.3).

- **Chapter 3** gives a simple account of the way in which our simulation programme, Finite-Difference Time Domain (FDTD), works to predict how the proposed metasurface devices will interact with electromagnetic radiation.

- **Chapter 4** will describe an investigation of the optimisation of the design for a metal-insulator-metal (MIM) metasurface beam-steering device. This was done by exploring the optical response of three different Drude-like metals in order to determine which materials were most suitable as the various metallic components of the metasurface. This device will employ spatially varied resonator elements in order to establish local phase control across the device surface. A metasurface beam-steerer is then proposed and investigated, which utilises the metals found to best enhance the device performance.

- **Chapter 5** will present the design and analysis of the performance of an alternative MIM metasurface beam-steering device. This device will employ a thermal gradient across the device surface in order to change the local environment of each resonator element, while maintaining a constant resonator geometry. An analogous device, which utilises both a thermal gradient and spatially varied resonator geometries, is also proposed and investigated. The performance of such a device is compared to those which only employ just one of these phase-modulating effects.

- **Chapter 6** will present an overview of the results and discuss the advantages and set-backs of the proposed structures. The limitations of plasmonic nanoscale metasurfaces are discussed, as well as the potential to overcome these impediments.

Chapter 2

2 Background & Theory

2.1 Surface Plasmons

As mentioned before, our primary focus is on plasmonic metasurfaces, consisting of metallic resonator elements. In order to understand the optical response of these elements when subject to electromagnetic radiation, one needs to consider the behaviour of the freely conducting electrons within the metal.

The free electron gas within these metallic nanoparticles can support surface and volume charge density oscillations when exposed to optical frequencies [23]. A restoring force is established due to the displacement of the electrons with respect to the positively charged lattice. This results in a certain plasmon resonance that has a dependence on the geometry of the nanoparticle.

Though this phenomena occurs within metallic nanostructures at optical frequencies (10 nm-$10^3\mu$m), one cannot re-create this effect with larger metallic structures at longer wavelengths, despite the scale invariance of Maxwell's equations. This is as the metal properties are vastly different at different frequencies.

2.1.1 Drude Model

Let us consider the Drude model as a first approximation to describe the behaviour of metals when subject to optical frequency radiation. The Drude model is similar to the Lorenz model, which treats charges in a material as harmonic oscillators [23, 33, 34]. An electric field interacts with the atoms in the metal as described by the following expression;

$$m\vec{a}_{el} = F_{E,Local} + F_{Damping} + F_{Spring} \tag{1}$$

This interaction is illustrated in Figure 1, and can be re-expressed as follows;

$$m\frac{d^2\vec{r}}{dt^2} + m\gamma\frac{d\vec{r}}{dt} + \alpha\vec{r} = -e\vec{E}_o e^{-i\omega t} \tag{2}$$

γ is the damping constant,

α is the spring constant,

ω is the frequency of the applied field,

E_o is the amplitude of the applied field.

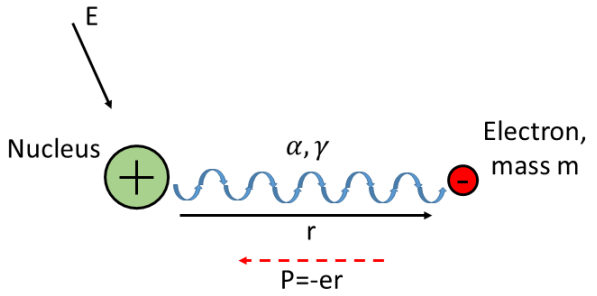

Figure 1: Lorentz (harmonic oscillator) model

The Drude model sets α=0, implying a system of free electrons (not bound to any nucleus). The mass in Equation 2 is now the effective mass of the free electrons.

$$m_e \frac{d\vec{v}}{dt} + m_e \gamma \vec{v} = -e\vec{E} \tag{3}$$

The current density is defined as $\vec{J} = -Ne\vec{v}$, where N is the number of electrons per unit volume. Subbing this into Equation 3 yields;

$$\frac{d\vec{J}}{dt} + \gamma \vec{J} = \frac{Ne^2}{m_e}\vec{E} \tag{4}$$

Assuming that the conduction current density and the applied electric field can be expressed in the form $\vec{J} = \vec{J}_o e^{-i\omega t}$ and $\vec{E} = \vec{E}_o e^{-i\omega t}$, respectively, than the following equation can be written;

$$\vec{J}(-i\omega + \gamma) = \frac{Ne^2}{m_e}\vec{E} \tag{5}$$

In the case of an applied oscillating field, where the static conductivity (σ) is defined as $(Ne^2)/(m_e\gamma)$, the current density can be expressed as follows;

$$\vec{J} = \left[\frac{\sigma}{1 - (\frac{i\omega}{\gamma})}\right]\vec{E} = \sigma_\omega \vec{E} \tag{6}$$

where σ_ω is the dynamic conductivity.

The above equation implies that for low frequencies (large λ), where $\omega/\gamma << 1$, the dynamic conductivity is real and the electrons are in phase with the applied field. However, if the frequency

of the applied field increases (lower λ), then the dynamic conductivity becomes complex. The electrons lag behind the applied electric field as a result of their inertia.

Further investigating the optical properties of metals, we can consider the wave equation from Maxwell's relations. Here, the permittivity of free space is ε_o, and the polarisation is assumed to be zero ($\vec{P} = 0$).

$$\Delta^2 \vec{E} = \frac{1}{c^2}\frac{\partial^2 \vec{E}}{\partial t^2} + \frac{1}{\varepsilon_o c^2}\frac{\partial \vec{J}}{\partial t} \tag{7}$$

Substituting in the expression for $\vec{J}$ yields;

$$\Delta^2 \vec{E} = \frac{1}{c^2}\frac{\partial^2 \vec{E}}{\partial t^2} + \frac{1}{\varepsilon_o c^2}\left[\frac{\sigma}{1-(\frac{i\omega}{\gamma})}\right]\frac{\partial \vec{E}}{\partial t} \tag{8}$$

Using the Ansatz $\vec{E} = \vec{E_o} e^{i(\vec{k}\cdot\vec{r}-\omega t)}$, as well as the relation $c^2 = 1/\varepsilon_o \mu_o$ giving the following expression for the wavenumber;

$$k^2 = \frac{\omega^2}{c^2} + i\left[\frac{\sigma\omega\mu_o}{1-(\frac{i\omega}{\gamma})}\right] \tag{9}$$

where μ_o is the permeability of free space.

From Equation 9, the dielectric function (refractive index squared) of the metallic medium can be obtained, since $n^2 = (c^2/\omega^2)k^2$, which can, in turn, give rise to the plasma frequency, ω_p.

$$\varepsilon_{Drude}(\omega) = n^2 = 1 + i\left[\frac{\sigma c^2 \mu_o}{\omega(1-\frac{i\omega}{\gamma})}\right] = 1 - \frac{\gamma\sigma c^2\mu_o}{\omega^2 + i\omega\gamma} = 1 - \frac{\omega_p^2}{\omega^2 + i\omega\gamma} \tag{10}$$

Here the plasma frequency squared can be expressed as $\omega_p^2 = \gamma\sigma c^2\mu_o = Ne^2/m_e\varepsilon_o$. This is the frequency at which the disrupted electrons oscillate around the equilibrium position. This oscillation is a result of the electrons displacement, from the uniform distribution of positive background ions, when subject to electromagnetic radiation. Though electric fields build up to restore the neutrality of the plasma, the inertia of the electrons cause them to overshoot their initial positions, leading to an oscillation with the characteristic plasma frequency. Intuitively, it is of no surprise that the plasma frequency is correlated to the carrier density.

For high frequencies, we can neglect the damping constant in Equation 10, resulting in $n^2 = 1 - \frac{\omega_p^2}{\omega^2}$. Evidently, when the metal is exposed to radiation with a frequency less than the plasma frequency ($\omega < \omega_p$), n is complex. In this case, the radiation is attenuated, which results in the high reflectivity of metallic surfaces. This phenomenon is seen in noble metals at optical frequencies. In contrast, incident frequencies that are greater than the plasma frequency ($\omega > \omega_p$) lead to real values of n, and therefore, transparent media.

2.1.2 Interband Transitions

Though the Drude model provides a good approximation for the dielectric constant of metals at higher optical wavelengths (i.e. in the infrared regime), is fails to support experimental values at lower wavelengths. This is as a metal is not exclusively composed of free electrons. Indeed, bound electrons exist in low-lying shells of the metallic atom [23, 33]. These bound electrons can be excited to the conduction band through absorption of high energy photons. The equation of motion of bound electrons is analogous to that of the Drude model, but takes the spring constant into account (i.e. the Lorenz model given in Equation 2). In this case, however, α is now the spring constant of the potential that keeps the bound electrons in place, and hereby denoted α_b. Similarly, $m_{e,b}$ and γ_b are the effective mass and damping constant of bound electrons, respectively. This damping constant primarily accounts for radiative damping.

$$m_{e,b}\frac{d^2\vec{r}}{dt^2} + m_{e,b}\gamma_b\frac{d\vec{r}}{dt} + \alpha_b\vec{r} = -e\vec{E}_o e^{-i\omega t} \tag{11}$$

Following the same procedure as before, we can compute the dielectric function due to the interband transition of bound electrons.

$$\varepsilon_{Interband}(\omega) = 1 + \frac{\tilde{\omega}_p^2}{(\omega_o^2 - \omega^2) + i\omega\gamma} \tag{12}$$

In this case, the plasma frequency squared is $\tilde{\omega}_p^2 = \tilde{N}e^2/m_{e,b}\varepsilon_o$, where $\tilde{N}$ is the density of bound electrons. This however, does not have the same physical meaning as ω_p, derived from the Drude model. The term ω_o, which is given by $\sqrt{\alpha_b/m_{e,b}}$, arises from the additional term in Equation 11, which accounts for the 'spring force'.

The most accurate way to model the dielectric function of metals is by considering both the free-electron model (for high wavelengths), and interband transitions (for low wavelengths). For example, the Drude model can effectively approximate the optical properties of gold above 650 nm wavelength [35]. However, below 650 nm, where the photons are more energetic, and therefore more interband transitions occur, the Drude model deviates from experimental observations.

2.1.3 Skin Depth

Another important thing to consider when utilising metallic optical resonators is the skin depth of the material. Going back to Equation 9, we can state that for small enough frequencies, such that

$k^2 \cong i\sigma\omega\mu_o$, the real and imaginary components of the wavenumber will be equal;

$$k_R = k_I = \sqrt{\sigma\omega\mu_o/2} \tag{13}$$

Since the skin depth is given by $\delta_e = 1/k_I$ [36], the following expression can be deduced;

$$\delta_e = \sqrt{\frac{2}{\sigma\omega\mu_o}} = \sqrt{\frac{2\varepsilon_o c^2}{\sigma\omega}} \tag{14}$$

δ_e can be considered as double the penetration depth, i.e. $\delta_e = 2\delta p$. Ohmic losses occur within this penetration depth, which is the primary disadvantage when working with metallic materials. For obvious reasons, it is desirable to minimise these Ohmic losses, which can be done by reducing the penetration depth. It is evident from Equation 14 that the skin depth, and thus the penetration depth, is a function of the material conductivity (σ). In turn, the conductivity is related to the dielectric function, see Equation 10. By selecting a material with a large, negative, real part of $\varepsilon(\omega)$, one can reduce the losses in metal nanoparticles.

Due to the intrinsic losses within metallic materials, many works have opted to use dielectric elements as the resonator component of their metasurface device [21, 37]. Dielectric optical resonators which support mode volumes can establish local electric and displacement field confinement, analogous to that of plasmonic resonators, with less intrinsic losses [37].

2.1.4 Metal-Insulator Interface

Consider a single interface between a metallic (conductor) and insulator (or dielectric) half-space, as shown in Figure 2. This is one of the most simple geometries in which surface plasmon polaritons (SPPs) arise. These SPPs are electromagnetic excitations which propagate at the interface between a dielectric and conductor. These excitations are evanescently confined in the perpendicular direction. These result from coupling between the electromagnetic fields and the oscillations of the electron plasma within the conductor material [38]. Let us investigate the propagating wave solutions confined to the interface [35, 39]. Since these are evanescent waves, they are exponentially decreasing in each material region.

Therefore, the component of the radiation propagating along the z-direction will have an addition factor of $e^{ik_z z}$ in the familiar equations for a monochromatic plane wave, describing the electric ($\vec{E}$) and magnetic ($\vec{H}$) field vectors;

$$\vec{E}(\vec{r},t) = \vec{E}e^{i\vec{k}\cdot\vec{r}-i\omega t} \quad \text{and} \quad \vec{H}(\vec{r},t) = \vec{H}e^{i\vec{k}\cdot\vec{r}-i\omega t} \tag{15}$$

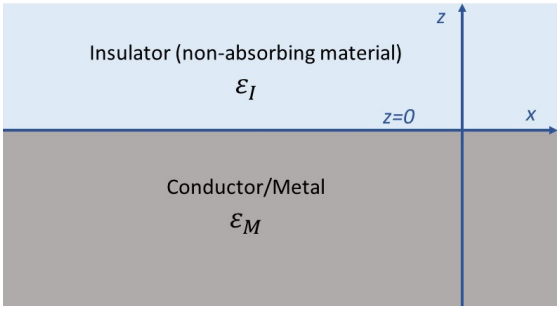

Figure 2: Metal-Insulator Interface

Since these SPP waves decay when propagating along the z-direction, the following constraint can be imposed; $|e^{ik_z z}| = e^{-Im(k_z)z} \rightarrow 0$ as $z \rightarrow \pm\infty$. In order for this to be satisfied, the following must apply;

$$Im(k_z) = \begin{cases} > 0 \text{ for } z > 0 \\ < 0 \text{ for } z < 0 \end{cases} \tag{16}$$

This means that the insulator material has positive real dielectric constant (ε_I), while the metallic region is described by a dielectric function ($\varepsilon_M(\omega)$) where the real component is less than zero, i.e. Re[ε_M]< 0.

Let us now consider the structure under p-polarisation illumination, i.e. transverse magnetic (TM) polarisation, where the magnetic field vector is parallel to the interface. In this situation, the plane of incidence may be the xz plane, resulting in $\vec{E}$ to be parallel to the xz plane, and $\vec{H}$ to be parallel to the y plane. The Maxwell equations below can be simplified to provide Equations 17-19, since $E_y = 0$, $H_x = 0$, and $H_z = 0$.

$$\Delta \text{ x } \vec{E}(\vec{r},t) = -\frac{\partial \vec{B}(\vec{r},t)}{\partial t} \quad \rightarrow \quad \partial_z E_x(\vec{r}) - \partial_x E_z(\vec{r}) = i\omega\mu_o H_y(\vec{r}) \tag{17}$$

$$\Delta \text{ x } \vec{H}(\vec{r},t) = -\frac{\partial \vec{D}(\vec{r},t)}{\partial t} \quad \rightarrow \quad -\partial_z H_y(\vec{r}) = -i\omega\varepsilon_o\varepsilon(\omega)E_x(\vec{r}) \tag{18}$$

$$\Delta \cdot \vec{D}(\vec{r},t) = 0 \quad \rightarrow \quad \varepsilon(\omega)\{\partial_x E_x(\vec{r}) + \partial_z E_z(\vec{r})\} = 0 \tag{19}$$

Keeping in mind the exponential decay in the z-direction at the metal-insulator interface, the solutions of Equations 17-19 can be expressed as;

$$F(\vec{r}) = F(x)e^{ik_z z} \tag{20}$$

where $F = E_i$ or $F = H_j$.

Using Equations 19 and 20, we can evaluate an expression for E_z as a function of E_x.

$$E_z(x) = -\frac{\partial_x E_x(x)}{ik_z} \tag{21}$$

Similarly, we can use Equations 18 and 20 to explicitly illustrate the relationship between H_y and E_x.

$$H_y(x) = \frac{i\omega\varepsilon_o\varepsilon(\omega)}{ik_z}E_x(x) \tag{22}$$

We can use these two expressions to deduce a new equations, which is only in terms of E_x. This can be done by subbing in Equations 21 and 22 into 17.

$$ik_z E_x(x) + \frac{\partial_x^2 E_x(x)}{ik_z} = -\frac{\omega^2\varepsilon_o\mu_o\varepsilon(\omega)}{ik_z} \tag{23}$$

Using the relation $1/c^2 = \varepsilon_o\mu_o$, Equation 23 can be re-expressed to give;

$$\partial_x^2 E_x(x) = -\left\{\left(\frac{\omega}{c}\right)^2\varepsilon(\omega) - K_z^2\right\}E_x(x) \tag{24}$$

where

$$K_x = \sqrt{\left(\frac{\omega}{c}\right)^2\varepsilon(\omega) - k_z^2} \tag{25}$$

which can be considered as the wave-vector of the x component. The general solution of Equation 24 can be expressed as;

$$E_x(x) = Ae^{+iK_x x} + Be^{-iK_x x} \tag{26}$$

where A and B are constants.

The signs indicate the propagation direction along the x-axis. Similarly, the x-component of the electric field in the insulator region ($z > 0$) and the metallic region ($z < 0$) can be expressed as, $E_x^I(x, y, z) = E_x^I(x)e^{ik_z^I z}$ and $E_x^M(x, y, z) = E_x^M(x)e^{ik_z^M z}$, respectively. Keeping in mind Maxwell's boundary condition, which states $H_y^I(x) = H_y^M(x)$ at $z = 0$, and Equation 22, the following expression can be deduced;

$$\frac{i\omega\varepsilon_o\varepsilon_I}{ik_z^I}E_x^I(x)|_{z=0} = \frac{i\omega\varepsilon_o\varepsilon_M}{ik_z^M}E_x^M(x)|_{z=0} \tag{27}$$

This can be simplified further when considering the other boundary condition, $E_x^I(x)|_{z=0} = E_x^M(x)|_{z=0}$, which yields;

$$\frac{\varepsilon_I}{k_z^I} = \frac{\varepsilon_M}{k_z^M} \tag{28}$$

By also recognising the boundary condition $K_x^I = K_x^M$ at $z = 0$, we can re-express the above equation in terms of K_x, giving the desired dispersion equation (DE) at the metal-insulator interface;

$$\frac{\varepsilon_I}{\sqrt{(\frac{\omega}{c})^2 - K_x^2}} = \frac{\varepsilon_M}{-\sqrt{(\frac{\omega}{c})^2 - K_x^2}} \tag{29}$$

Note that the convention of the sign in the above equation is due to the constraints imposed by 16, reminding us that surface waves are only induces at the boundary between materials with opposite signs in their real dielectric permittivities, i.e. the boundary between a conductor and an insulator (or any non-absorbing material).

To better illustrate the relationship between K_x and ω (and ω-dependent terms), we can easily modify Equation 29 to yield;

$$K_x = \frac{\omega}{c}\sqrt{\frac{\varepsilon_M(\omega)\varepsilon_I}{\varepsilon_M(\omega) + \varepsilon_I}} \tag{30}$$

The above expression is valid for metallic materials with and without attenuation, where ε_M contains real and complex components.

Before we use Equation 30 to investigate the realistic behaviour of SPPs at the Ag-air interface, let us first consider the idealised scenario, where the conductor permittivity is equated to the real-valued Drude permittivity;

$$\varepsilon_M = 1 - \left(\frac{\omega_p}{\omega}\right)^2 \tag{31}$$

Approximating $\varepsilon_I = 1$, (i.e. for air), Equation 30 can be re-arranged to solve for ω;

$$\omega = \sqrt{\frac{\omega_p^2 + 2(K_x c)^2}{2} \pm \frac{\sqrt{\omega_p^4 + 4(K_x c)^4}}{2}} \tag{32}$$

Plotting $\hbar\omega$ against $K_x\hbar c$ (Figure 3), the SPP dispersion with negligible interband damping can be visualised.

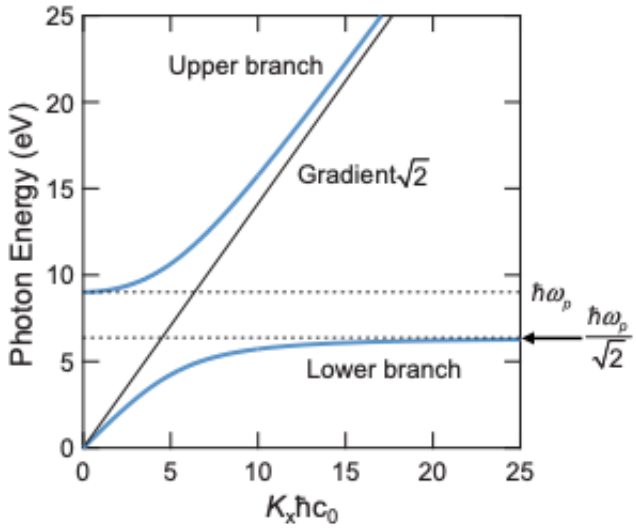

Figure 3: SPP dispersion diagram assuming a pure Drude-metal (Ag)-air interface

Reprinted with permission from [35]

Evidently, the SPP dispersion forms two branches, where the upper and lower branches for Ag corresponds to the plus and minus within the square root of Equation 32, respectively. Radiation into the silver occurs where $\omega > \omega_p$, where the material becomes transparent. This upper branch can thus be considered as the radiative mode. This branch is not actually considered a surface wave, but a transverse wave, since ε_M here is positive, as well as real. The branch lies outside, and becomes asymptotically close to the light cone, where $\omega/c = \sqrt{2}K_x$, and is excited by far-fields.

In contrast, the lower branch, or bound mode, lies within the light cone, and asymptotically approaches the surface plasmon frequency, $\omega_{sp} = \omega_p/\sqrt{2}$ as $K_x \to \infty$. In this high wavevector regime, the group velocity, defined by $v_g = \partial\omega/\partial K_x$, approaches zero (i.e. $v_g \to 0$). Unlike the radiative mode, this mode can be considered as a surface plasmon, one with electrostatic properties. This feature is not observed in reality however, as conduction electron oscillations (interband transitions) cannot be ignored in real systems. In the region where the energy values are low, and the wavevectors are small, the SPP propagation constant is very close to the light cone, within the insulator material. This is illustrated over a wide wavelength range, and is known as Sommerfeld-Zenneck waves [40]. Separating the two modes is an energy gap, where the propagation of the surface wave is prohibited.

Though Figure 3 is useful in illustrating various properties of SPP dispersion, we now want to investigate a more realistic system, where we eliminate the assumption that $Im(\varepsilon_M) = 0$, thus including both interband transitions as well as the free-electron system. Figure 4 uses Equation 30 to depict the behaviour of the dispersion at an Ag-air interface, but does not assume silver to be a purely Drude-like metal.

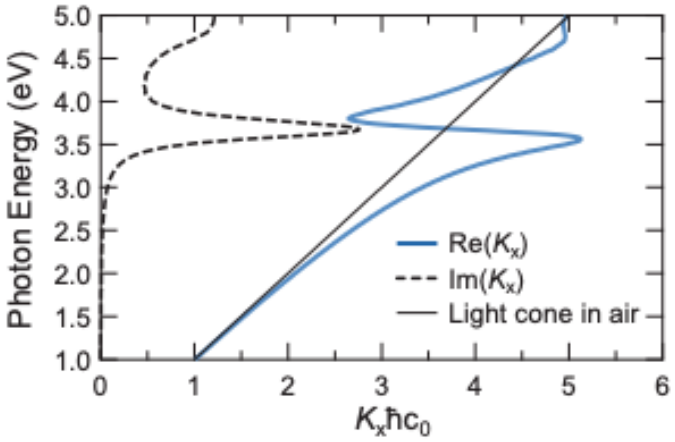

Figure 4: SPP dispersion diagram of actual metal (Ag)-air interface

Reprinted with permission from [35]

The above figure is analogous to Figure 3, the SPP dispersion is real, and in close proximity to the light cone at energy values below 2.0 eV (wavelengths above $\approx$ 620 nm). However, the distinction in Figure 4 is depicted above 2.0 eV, where the Im(K_x) emerges and increases as the energy approaches 3.8 eV, due to the interband transitions. Since the peak of Im(K_x) occurs at 3.8 eV, the oscillation strength of the interband transition is large here. The bound SPPs now exhibits a finite wavevector at the surface plasmon frequency (ω_{sp}), conveying a lower bound on the wavelength of the surface plasmon, i.e. $\lambda_{sp} = 2\pi/Re(K_x)$. It is also interesting to note the backward surface wave propagation in the $-K_x$ direction from 3.6 eV to 3.8 eV, despite incident light exhibiting a positive wavenumber ($+K_x$). Therefore, the group velocity of the interface wave is negative within that energy range ($v_g < 0$).

2.1.5 Mass & Spring Model

Now that we have investigated some of the main properties of metals at optical frequencies, as well as the emergence of SPPs at the boundary between conductors and insulators, let us look at a model describing the plasmonic resonance within metallic nano-particles. We can apply a simple mass-and-spring model in order to explore the relationship between the particle resonance frequency and its geometry [41].

Let us consider an elongated, cylindrical particle, as shown in Figure 5. Here we are assuming the electron cloud within the particle is displaced by δx. Opposite point charges have accumulated on either side of the particle, where the charge magnitude is determined by $q = NeA\delta x$, i.e. it is a function of the cross-sectional area (A), and the charge carrier density (N). The Coulomb potential energy of the accumulated charge is given by;

$$W(\delta x) = \frac{1}{4\pi\varepsilon_o}\frac{q^2}{d} = \frac{1}{4\pi\varepsilon_o}\frac{(NeA)^2}{d}(\delta x)^2 \tag{33}$$

The restoring force can now be obtained. Equation 34 below conveys the linear relationship between the displacement of the electron cloud, and the restoring force. Our system can therefore be considered as a harmonic oscillator.

$$F(\delta x) = \frac{\partial W(\delta x)}{\partial(\delta x)} = -\frac{1}{2\pi\varepsilon_o}\frac{(NeA)^2}{d}\delta x = -\alpha\delta x \tag{34}$$

where α = elastic constant of the restoring force.

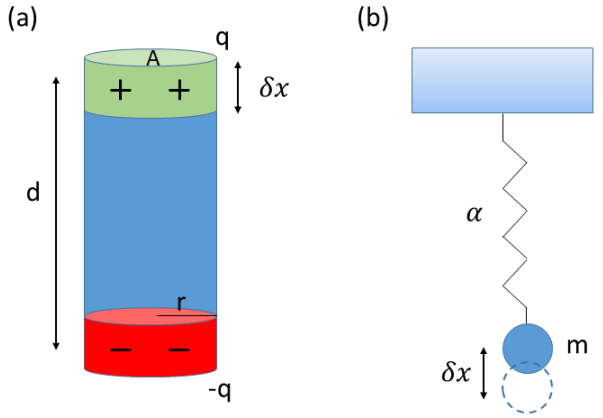

Figure 5: Schematic of mass and spring model of single plasmonic particle

Figure reproduced from [33]

Defining the resonance frequency of the plasmonic structure to be $w_{res} = \sqrt{\alpha/m}$, where m is the total effective mass of the electron system, we can now use Equation 34 to derive an expression that relates the resonance frequency to the geometric parameters of the particle.

$$\alpha = \frac{(Ne)^2}{2\pi\varepsilon_o}\frac{A^2}{d} \tag{35}$$

Therefore,

$$w_{res} = \sqrt{\frac{(Ne)^2}{2\pi\varepsilon_o}\frac{A^2}{d}\frac{1}{m}} \tag{36}$$

Using the plasma frequency defined in Section 2.1.1, and by expressing the total effective mass of the system in terms of the effective electron mass, $m = Nm_eAd$, as well as the cross-sectional area of the particle as $A = \pi r^2$, one can depict the resonance frequency as;

$$w_{res} = w_p\sqrt{\frac{r^2}{2d^2}} \tag{37}$$

Defining the aspect ratio of the particle to be $R = d/2r$ we can now state;

$$w_{res} = \frac{w_p}{2\sqrt{2}}\frac{1}{R} \tag{38}$$

Equation 38 above illustrates the inverse relationship between the resonance frequency and the aspect ratio of the metallic particle. Although the above equation is less accurate for shorter and thicker particles due to the assumption that the charges are point-like, it clearly conveys how the geometry of the particle is responsible for its resonance frequency, and therefore its phase response when exposed to electromagnetic radiation. In a metasurface, the phase of the scattered light will vary around the resonance wavelength of the resonator element, analogous to the way in which the phase of an oscillator varies with respect to its detuning from resonance (see Figure 8b). By changing the resonant frequency of the element, i.e. by changing its geometry, one can gain control of the phase of the reflected or transmitted light from the metasurface.

2.1.6 Two-Wire Resonators

One can describe how the surface charges of two neighbouring metallic resonators interact by employing a coupled-harmonic oscillator model [33], i.e. by introducing an additional 'spring' between two end-to-end particles, as seen in Figure 6.

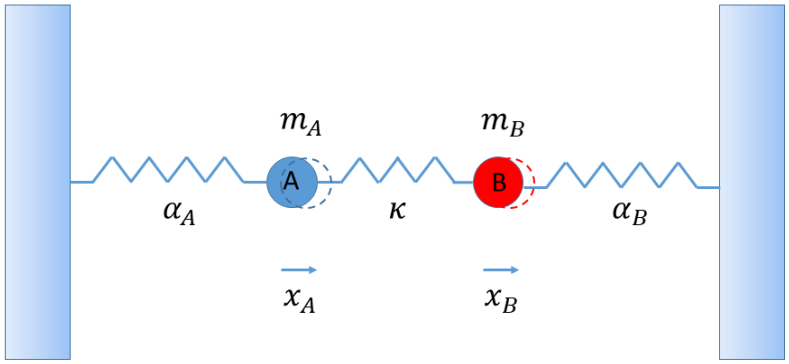

Figure 6: Schematic of two-wire resonators

Figure reproduced from [42]

Neglecting coupling ($\kappa = 0$), particle A and B have eigenfrequencies $w_A^o = \sqrt{\alpha_A/m_A}$ and $w_B^o = \sqrt{\alpha_B/m_B}$, respectively. If $\kappa \neq 0$, the equations of motion for both particle A and B can be expressed as;

$$m_A\ddot{x}_A + \alpha_A x_A + \kappa(x_A - x_B) = 0 \tag{39}$$

$$m_B\ddot{x}_B + \alpha_B x_B - \kappa(x_A - x_B) = 0 \tag{40}$$

The solution to the above equations can be written in the form $x_i(t) = x_i^o e^{-iw_\pm t}$, where $w_\pm$ are the new in-phase and out-of-phase eigenfrequencies. By defining;

$$w_A = \sqrt{(\alpha_A + \kappa)/m_A} \quad \text{and} \quad w_B = \sqrt{(\alpha_B + \kappa)/m_B} \tag{41}$$

and

$$\Gamma = \frac{\sqrt{\kappa/m_A} \cdot \sqrt{\kappa/m_B}}{\sqrt{w_A w_B}} \tag{42}$$

we can use our solution to determine these eigenfrequencies to be;

$$w_\pm^2 = \frac{1}{2}\left[w_A^2 + w_B^2 \pm \sqrt{(w_A^2 - {w_B}^2)^2 + 4\Gamma^2 w_A w_B}\ \right] \tag{43}$$

We can compare the behaviour of these new eigenfrequencies to our original frequency values, where the motion of the two particles were independent of each other. Figure 7a below illustrates the frequencies, when varying the elastic constants, of the two particles in the absence of coupling. Here we set $\alpha_A = \alpha_o$, $\alpha_B = \alpha_o + \Delta\alpha$, and $m_A = m_B = m_o$. Whiles it's obvious the frequency

of particle A's oscillation is constant, the graph depicts the increase of w_B^o from 0 to $\sqrt{2} \cdot w_o$, where $w_o = \sqrt{\alpha_o/m_o}$, as $\Delta\alpha$ varies from $-\alpha_o$ to $+\alpha_o$. The two curved intersect when $\Delta\alpha = 0$. This crossing characteristic is lost in the presence of strong coupling between the particles, as seen in Figure 7b. This frequency splitting can be defined by $\Gamma = [w_+ - w_-]$, which increases with the coupling strength (κ), as dictated by Equation 42. This coupling strength is increased with decreased distance between the two metallic particles.

This coupling between two wire elements over a narrow gap can result in an enhanced, localised optical near-field within the gap. This near-field coupling between densely packed resonator elements may lead to digressions from the expected performance of the metasurface device. Simulations often determine the device performance by looking at the response of each individual element, which, as highlighted in the above argument, is different to the behaviour of strongly coupled systems. However, many simulations do take into account near-field coupling between neighbouring resonator elements before designing an appropriate device, as is the case in this thesis. They often do so by imposing periodic boundary conditions within the simulation software to replicate the effects of multiple resonator elements in close proximity.

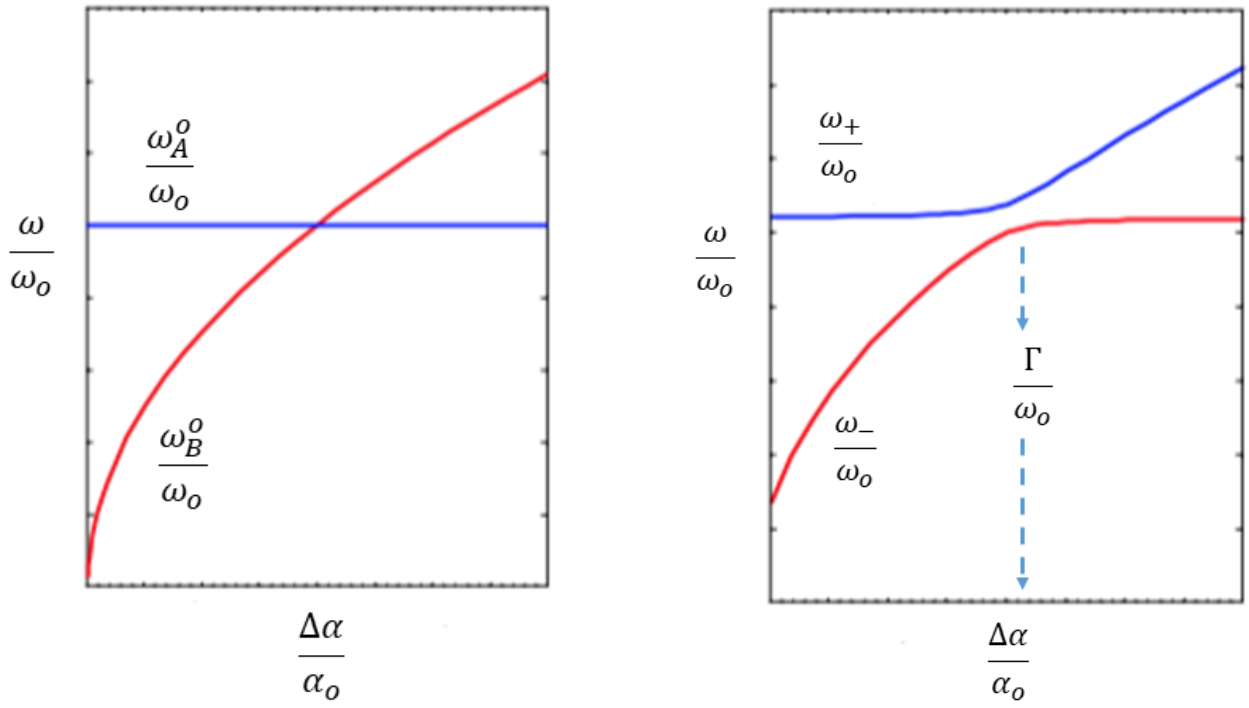

(a) Eigenfrequencies of uncoupled wire resonators

(b) Eigenfrequencies of coupled wire resonators

Figure 7: Eigenfrequencies of uncoupled and coupled resonator elements

Figure reproduced from [42]

2.1.7 Phase & Amplitude Response of Wire Resonators

As previously mentioned, the oscillations of the electron system within the metallic nano-wire can be described as a damped-driven harmonic oscillator, see Equation 2. As is the case with all harmonic oscillators, each nano-wire resonator will have an amplitude response and a phase response. The phase response is of particular importance when considering a metasurface device which attempts to utilise a spatially varying phase gradient in order to control the propagation path of reflected or transmitted radiation.

When attempting to analytically describe the amplitude and phase response of each optical resonator, the incident field can be considered as the driving force in the traditional damped-driven harmonic oscillator equation, whereas the mass (m) can be considered the effective electron mass of the system. The equation below re-iterates Equation 2 in Section 2.1.1;

$$m\dddot{r} + m\gamma\ddot{r} + \alpha r = -eE_o e^{i\omega t} \tag{44}$$

where ω is the frequency of the incident light.

We can try $r = Ae^{i\omega t}$ as a solution to Equation 44, where A is the amplitude of the oscillation of the electron system. This yields the following expression;

$$-m\omega^2 A + i\omega\gamma A + \alpha A = -eE_o \tag{45}$$

This can be re-expressed to give an equation for the amplitude of the oscillating electron system.

$$A = \frac{-eE_o}{\alpha - m\omega^2 + i\omega\gamma} \tag{46}$$

Dividing each term by m, and again noting the expression for the resonant frequency of the system, $\omega_{res} = \sqrt{\alpha/m}$, Equation 46 becomes;

$$A = \frac{-eE_o/m}{(\omega_{res}^2 - \omega^2) + i(\omega\gamma/m)} = \frac{E_o/m \cdot [(\omega_{res}^2 - \omega^2) - i\omega\gamma/m]}{(\omega_{res}^2 - \omega^2)^2 + (\omega\gamma/m)^2} \tag{47}$$

Since we are interested in the real part of Equation 47, it is worth noting the expression $x+iy = ze^{i\phi}$, where $z = \sqrt{x^2 + y^2}$ and $tan\ \phi = y/x$. Applying this mathematical statement, we obtain;

$$(\omega_{res}^2 - \omega^2) - i\omega\gamma/m = \sqrt{(\omega_{res}^2 - \omega^2)^2 + (\omega\gamma/m)^2} \cdot e^{i\phi} \tag{48}$$

We can use Equation 48 to replace the equivalent term in Equation 47. The particular solution, r_p, of our damped-driven harmonic oscillator system is;

$$r_p = Re\{Ae^{i\omega t}\} = Re\left\{ \frac{-eE_o/m\sqrt{(\omega_{res}^2 - \omega^2)^2 + (\omega\gamma/m)^2)} \cdot e^{i\phi}}{(\omega_{res}^2 - \omega^2)^2 + (\omega\gamma/m)^2} \cdot e^{i\omega t} \right\} \tag{49}$$

$$\therefore \quad r_p = \frac{-eE_o/m}{\sqrt{(\omega_{res}^2 - \omega^2)^2 + (\omega\gamma/m)^2}} \cdot cos\ (\omega t + \phi) \tag{50}$$

The real part of the amplitude response of the harmonic oscillator is therefore given by the following expression;

$$A = \frac{-eE_o/m}{\sqrt{(\omega_{res}^2 - \omega^2)^2 + (\omega\gamma/m)^2}} \tag{51}$$

while the phase response is given by;

$$tan\ \phi = \frac{\omega\gamma}{m(\omega_{res}^2 - \omega^2)} \tag{52}$$

Figure 8 below provides a visual representation of the relationship between the phase and amplitude of a harmonic oscillator and the incident frequency. It is evident from the figure that the phase

of light will vary around the resonant frequency of the oscillator (or optical element). Since we have already established that the resonant frequency is dependent on the physical dimensions of the resonator nano-wire, see Section 2.1.5, the resonant frequency of each element can be adjusted by changing its geometry.

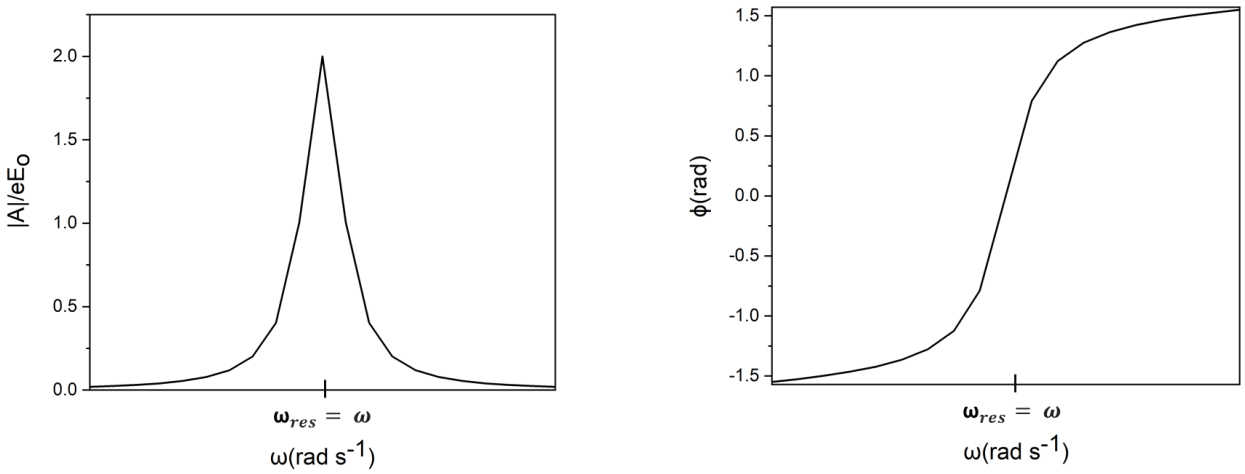

(a) Amplitude response

(b) Phase response

Figure 8: Phase and Amplitude response of damped-driven harmonic oscillator

2.2 Fermat's Principle

Previously, we have stated that the phase of light varies as a result of detuning the optical elements from their resonant frequency. This allows for abrupt phase shifts along the optical path, over the scale of the wavelength. The way in which this phase shift presents control over the propagation path of scattered light can be understood through Fermat's principle.

Fermat's principle, also known as the principle of least time, states that a ray of light will take the path that can be traversed in the least time when traveling between two points A and B; $\int_A^B n(\vec{r})dr$, where $n(\vec{r})$ is the local refractive index [24]. However, this statement is slightly incorrect. A more accurate version of the principle is to state that, if one were to make a slight adjustment to a travelling ray of light, there will only be a second-order change in the time the light ray would have taken if no such change was made. Therefore, a light ray would travel along a path such that there are other paths, infinitesimal near, which take the same amount of time (to a first-order approximation). A way to visually illustrate the relationship between the probability of

a photon travelling from a point A to a point B, and Fermat's principle of least time, was elegantly presented in one of Richard Feynman's lectures in optics [43]. Feynman devised a scenario where a light ray was travelling from a point A towards a point B, where it is already known that the path of least time is through an intermediate point C, see Figure 9a. The properties of any path that the ray can take can be described by a complex vector, $\rho e^{i\theta}$, where the angle θ describes the phase of the ray, and is proportional to the time that path requires. Every available path has its own complex vector, which is added onto each other, as conveyed in Figure 9b below. The overall probability of the photon travelling from A to B is proportional to the square of the length of the final vector.

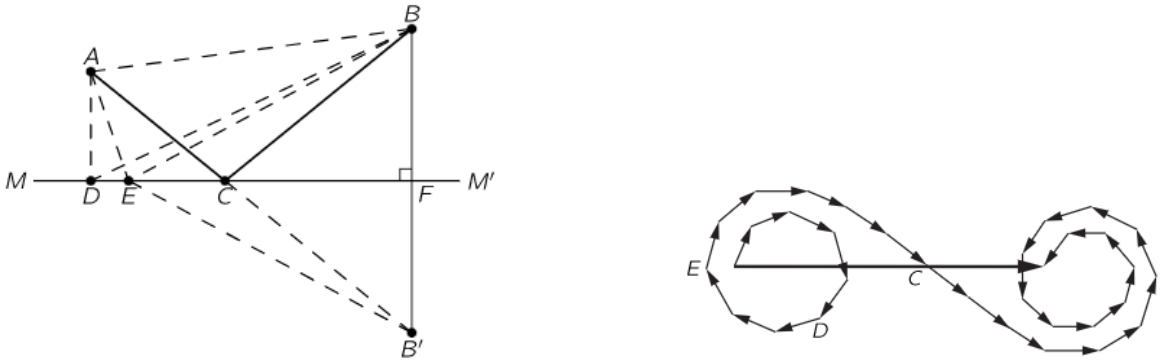

(a) Ray Diagram (b) Vector Diagram

Figure 9: Ray and vector diagrams illustrating Fermat's principle and the summation of the probability amplitudes for many neighbouring paths

Reprinted with permission from [43]

Looking at the leftmost spiral end of the diagram, consisting of paths with intermediate points far from C, it is evident that each consecutive path exhibits very different travel times, since the angles of the composite vectors are very different. However, as the optical path approaches C, the vectors become more similar, with almost identical angles (phases). These vectors again change gradually the further they get from C, forming another spiral of vectors in the far right. The probability amplitudes of the vectors making up the rightmost spiral are equal to the corresponding vectors making up the leftmost spiral, with opposing direction however. Therefore, when obtaining the total probability, the two ends of the vector diagram cancel each other out, leading to virtually no contribution from paths which exhibit very different travel times from each other. Fermat's

principle of least time is satisfied, as the resultant probability occurs only in the region where the vectors are pointing in the same direction, i..e. have the same angle or phase. Hence, the principle of least time can also be considered as the principle of stationary phase, i.e. the derivative of the phase accumulated along the real optical path, $\int_A^B d\phi(\vec{r})$, is zero with respect to infinitesimal changes of the path.

2.2.1 Snell's Generalised Law

From the principle of stationary phase defined above, one can deduce the generalised Snell's law for reflection and refraction [44]. This law illustrates the relationship between the phase variation along the surface of a boundary between two media, and the angle of reflection or transmittance from that boundary. Figure 10 below depicts two light rays traversing a boundary separating two different media, one with refractive index n_i, and the other with refractive index n_t.

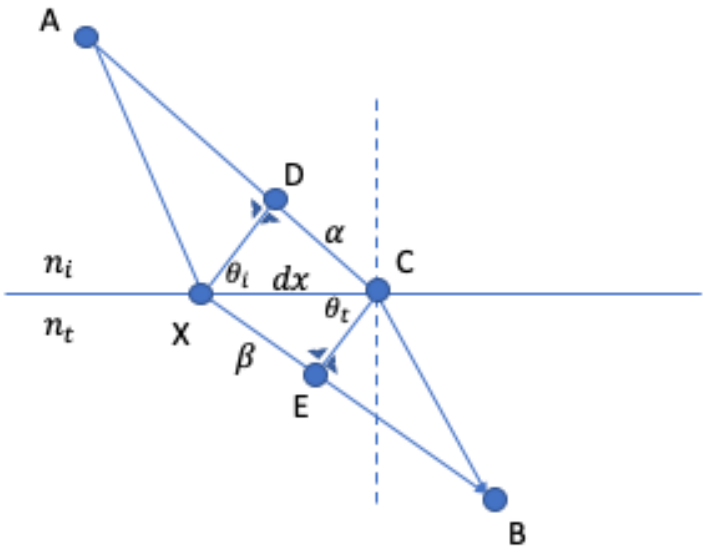

Figure 10: Schematic to derive the generalised Snell's law

Figure reproduced from [24]

These light rays are separated by an infinitesimally small distance dx. The ray travelling from point A to point X displays an abrupt phase shift ϕ at the point of interception. Similarly, the second ray, from point A to point C, displays a phase shift of $\phi + d\phi$. Since the separation between the two rays is infinitesimally small, the principle of stationary phase claims that the phases of the

two interceptions are equivalent. Additionally, the time it takes for the two rays to reach point B should be considered equal, therefore, we can draw a perpendicular line from point D to point X, and a perpendicular line from point E to point C, to show that the lengths DC (hereby denoted as α), and XE (hereby denoted as β), are equal.

$$k_o n_i \alpha = k_o n_t \beta \tag{53}$$

where the wave number, $k_o = 2\pi/\lambda_o$ (λ_o being the wavelength of free space).

Basic geometry offers two additional relationships, $sin(\theta_i) \cdot dx = \alpha$ and $sin(\theta_t) \cdot dx = \beta$, where θ_i and θ_t are clearly presented to be the angles of incidence and refraction, respectively. Keeping in mind that $\phi = \phi + d\phi$, the following relation can be computed;

$$k_o n_i sin(\theta_i) \cdot dx + (\phi + d\phi) = k_o n_t sin(\theta_t) \cdot dx + \phi \tag{54}$$

Therefore, the generalised Snell's law for refraction is,

$$sin(\theta_t) n_t - sin(\theta_i) n_i = \frac{\lambda_o}{2\pi} \frac{d\phi}{dx} \tag{55}$$

Similarly, the generalised Snell's law for reflection is,

$$sin(\theta_r) - sin(\theta_i) = \frac{\lambda_o}{2\pi n_i} \frac{d\phi}{dx} \tag{56}$$

where θ_r is the angle of reflection.

Equation 56 above highlights the nonlinear relationship between θ_r and θ_i. It is important to note that, in theory, all impinging radiation is transferred into anomalous reflection and refraction, since ϕ is a continuous function of the position along the boundary. However, actual experiments see the use of discrete optically thin resonators to realise these phase shifts along the interface between two media, meaning that radiation can also be reflected and refracted in accordance with the conventional Snell's law, i.e. where $d\phi/dx = 0$. Thus, the separation between these resonators has an implication on the efficiency of the metasurface device.

2.3 Vanadium Dioxide (VO_2)

The transition metal oxide known as vanadium dioxide (VO_2) is a key component of the metasurface devices proposed in this thesis, see Sections 4 and 5. The inclusion of VO_2, or indeed any phase

change material (PCM), allows for dynamic tunability of the scattered radiation from the devices, post-fabrication. This will be demonstrated later on.

In the 1950s, a great interest in the metal-to-insulator transition (MIT) in oxides was instigated, largely due to a paper published by Morin [45]. This excitement was further encouraged by relevant discoveries that highlighted the potential of MIT oxides to be utilised in a wide variety of applications. As Morin mentioned, some MIT oxides show a drastic change in certain material properties due to heating or cooling across the transition temperature (T_{MIT}). For example, the electrical resistance of vanadium oxides (such as vanadium monoxide (VO), dioxide (VO_2), and sesquioxide (V_2O_3)) can change by several orders of magnitude [28, 45]. In addition, VO_2 also demonstrates a significant change in its optical properties (refractive index and extinction coefficient) when it transitions from its monoclinic to its rutile state, see Figure 25 in Section 5.2. These impressive changes in material properties occur at a low transition temperature ($\approx 340K$ in bulk crystals) relative to other PCMs, as previously mentioned in Section 1.1. The timescale of this transition is shown to be in the picosecond range by multiple experiments using various measuring techniques, such as optical pump-probe [46, 47], time-resolved x-ray diffraction [48, 49], and terahertz spectroscopy [50, 51]. A transition to the higher resistance state caused by Joule heating could take longer, of the order of one hundred nanoseconds, in accordance with heat dissipation time [52].

There exist many models to try and describe why these MIT transitions occur. One such model, known as Mott's theory [53, 54], states that every one of these materials has a unique critical carrier density (n_c), which is related to the Bohr radius (a_H) of the material by the expression $n_c^{1/3} \cdot a_H \approx 0.2$. A phase transition is said to occur, due to a process known as correlation (electron-electron interactions), once the charge carrier density is greater than n_c. Materials which seem to follow this type of transition are known as Mott-Hubbard insulators. However, some MIT have been found to occur as a result of electron-phonon interactions, known as Peierls MIT [55]. In this situation, materials exhibit a band structural change due to lattice deformations, which alters the material's periodic ionic potential and thus results in the band structural change.

The mechanism in which VO_2 undergoes a MIT has been long under debate. Along with the drastic changes in material properties discussed above, VO_2 undergoes a physical structural change from a monoclinic (MoO_2) insulating phase (M_1) to a rutile (tetragonal) metallic phase (R). This structural change maybe the cause of the MIT that occurs in VO_2, making it a Peierls type material.

However, its possible this structural change just accompanies a charge carrier-induced MIT, in which case VO_2 would be classified as a Mott-Hubbard type material. In the 1970s, band-splitting alignment analysis performed by Zylbersztejn and Mott [56] lead to the suggestion that VO_2 may not be a simple Mott-Hubbard insulator. The idea that VO_2 was not a Mott-Hubbard insulator was later supported by later works [57] in the 1990s. Local density approximation calculations on the monoclinic structure of VO_2 depicted a very small number of carriers, leading them to believe VO_2 was more likely a band insulator. Contributions from other works [58] led to slightly different insights, but also concluded that the M_1 phase of VO_2 is not the Mott-Hubbard type, though the exact nature of the transition is yet to be completely agreed upon.

Although the application of heat is possibly the most frequently used technique to trigger the phase transition in VO_2, there are numerous other methods which can be exploited. These include strain [59], magnetic [60], optical [60, 61] and electrical excitations [60, 62].

Chapter 3

3 Simulation Method

The metasurface devices presented in Sections 4 and 5 were simulated using finite-difference time domain (FDTD) Lumerical simulations. FDTD is a computational modelling technique which can be used to solve complex electromagnetic problems involving Maxwell's equations. This numerical analysis technique is widely used in various scientific disciplines that involve electrodynamics. It was first proposed by K.S. Yee [63] in 1966, and was later improved by Taflove in the 1970s [64, 65].

FDTD works by discretising Maxwell's curl equations using the central difference approximation, in both the time and spatial domains [66]. This provides an advantage over simulations that only approximate solutions to systems of differential equations in the frequency domain, as they are ineffective in modelling transient phenomena. After these curl equations are discretised, a leapfrog scheme is used to determine the electric and magnetic field distribution at each time step. This provides visualisations of the interaction between electromagnetic radiation and matter. FDTD has been used in various past works to compute the phase response, and therefore angle of reflection/transmission, of metamaterials [2, 3, 12]. In many cases, the obtained theoretical results are demonstrated to be excellent approximations of the corresponding fabricated devices [2].

When setting 3D simulations, a 3D grid is used. This grid is composed of unit cells, where the electromagnetic fields are located. The length, width and height of a unit cell are denoted Δx, Δy, and Δz, which are known as the resolution parameters. In general, the length of the resolution parameters are very similar to each other, which minimises potential issues during simulations. The grid is known as a co-located grid when the field components are located at a common point within the cell, e.g. at the origin. Though this set-up seems intuitive, there are multiple issues with this method, including the inability to satisfy the boundary condition of Maxwell's equations. In addition, co-located grids do not render the divergence equations as zero when trying to resolve the electric and magnetic field distributions. An alternative, and more effective method is the Yee grid, which staggers our field components throughout the unit cell. In this type of grid, each field components is set in a different location around the unit cell, as shown in Figure 12. Each field component is also offset from the origin by half the unit cell. In contrast to the co-located grid set-up, the Yee grid can neglect the divergence equations when approximating the curl operation

with finite differences, i.e. $\Delta \cdot (\varepsilon \vec{E}) = 0$, and $\Delta \cdot (\mu \vec{H}) = 0$.

Maxwell's curl equations are slightly modified in these operations, due to the presence of a normalisation factor; $\vec{H}_n = \sqrt{\mu_o/\varepsilon_o} \cdot \vec{H}$. This factor is necessary as the amplitude of the electric and magnetic field vectors can differ by several orders of magnitude. If this substantial difference is left unaddressed, the program may incorporate random rounding errors within its calculations, jeopardising the accuracy of the simulation. The more 'numerically-robust' curl equations are expressed as;

$$\Delta \text{ x } \vec{E} = \frac{-\mu_r}{c} \frac{\partial \vec{H}_n}{\partial t} \quad \text{and} \quad \Delta \text{ x } \vec{H}_n = \frac{\varepsilon_r}{c} \frac{\partial \vec{E}}{\partial t} \tag{57}$$

Assuming a diagonal isotropic material (i.e., $\epsilon_{ij} = 0$ and $\mu_{ij} = 0$, where $i \neq j$), Equations 57 can be expanded into six partial differential equations that are a function of both time and space. We will representatively convert the first partial derivative of the electric field equation, and the first partial derivative of the magnetic field equation, into finite difference form.

The first partial electric field equation (the H_x equation) can be written as;

$$\frac{\partial E_z}{\partial y} - \frac{\partial E_y}{\partial z} = \frac{-\mu_{xx}}{c} \frac{\partial H_{n,x}}{\partial t} \tag{58}$$

where μ_{xx} is the permeability at the same position as H_x in the Yee grid.

The above equation is composed of two spatial partial derivatives (left) and one partial derivative in time (right). We can first estimate the spatial derivatives in the right using the central finite difference method. Figure 12a below provides a visual representation of the operation. The left-hand side of Equation 58 now becomes;

$$\frac{E_z^{i,j+1,k}|_t - E_z^{i,j,k}|_t}{\Delta y} - \frac{E_y^{i,j,k+1}|_t - E_y^{i,j,k}|_t}{\Delta z} = \frac{-\mu_{xx}^{i,j,k}}{c} \frac{\partial H_{n,x}^{i,j,k}}{\partial t} \tag{59}$$

Note that every term in the above equation is evaluated at the same time-step (t). The first term depicts the E_z component from the next adjacent unit cell (faint blue arrow in Figure 12a being subtracted from the E_z component from the original cell (solid blue arrow in Figure 12a, as these two components surround the H_x component of the magnetic field. This difference is then divided by the distance between them (Δy). This procedure is repeated in the second term, now focusing on the other two electric field components surrounding the H_x component of the magnetic field, i.e. the E_y component from the above unit cell and the E_y component from the original unit cell.

Now that we have approximate solutions for the spatial derivative terms, let us now focus on the time derivative on the right hand side of Equation 59. In order to do this, we need to know how the $\vec{E}$ and $\vec{H}$ fields are defined to be separated by half a time step. We want to compute the derivative of H_x with respect to time, so as to conserve the time-step in each of the terms in our equation. To ensure the derivative is defined at $E_\alpha|_t$ (where α is either x, y or z), we must get the difference between H_x at $t + \Delta t/2$ and H_x at $t - \Delta t/2$, as illustrated in the schematic below.

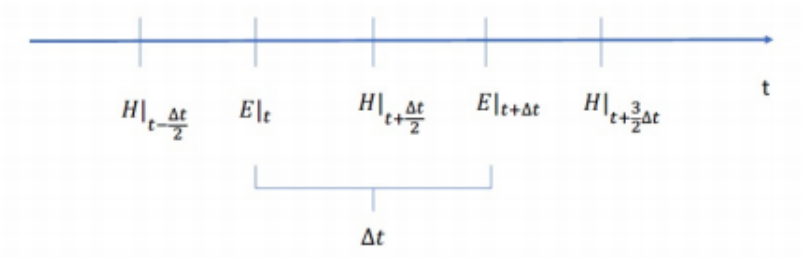

Figure 11: Leapfrog Diagram

Equation 59 can now be re-expressed as;

$$\frac{E_z^{i,j+1,k}|_t - E_z^{i,j,k}|_t}{\Delta y} - \frac{E_y^{i,j,k+1}|_t - E_y^{i,j,k}|_t}{\Delta z} = \frac{-\mu_{xx}^{i,j,k}}{c} \frac{H_{n,x}^{i,j,k}|_{t+\Delta t/2} - H_{n,x}^{i,j,k}|_{t-\Delta t/2}}{\Delta t} \tag{60}$$

The coupled scalar differential equation 58 has now been converted into a finite difference equation 60, by discretising the equation in both space and time. The above equation is much easier to deal with.

We can discretise the first partial magnetic field equation (the E_x equation) in a similar fashion. As illustrated by Figure 12b, the two field components that are to be used in the central finite difference method are H_z and H_y of the original unit cell, H_y of the below unit cell, and H_z of the previous adjacent unit cell. These are the components of the magnetic field which surround the E_x component of the electric field. Using the same leapfrog time scheme portrayed by Figure 11, the finite difference E_x can be computed.

$$\frac{H_{n,z}^{i,j,k}|_{t+\Delta t/2} - H_{n,z}^{i,j-1,k}|_{t+\Delta t/2}}{\Delta y} - \frac{H_{n,y}^{i,j,k}|_{t+\Delta t/2} - H_{n,y}^{i,j,k-1}|_{t+\Delta t/2}}{\Delta z} = \frac{\varepsilon_{xx}^{i,j,k}}{c} \frac{E_x^{i,j,k}|_{t+\Delta t} - E_x^{i,j,k}|_t}{\Delta t} \tag{61}$$

This computation can be repeated for the other four scalar differential equations obtained from Equations 57. The program can purposefully neglect to simulate electromagnetic propagation in

certain directions, depending on whether the simulation is in 1D, 2D or 3D space. Selecting a lower dimension may save considerable simulation time, however, less information is represented.

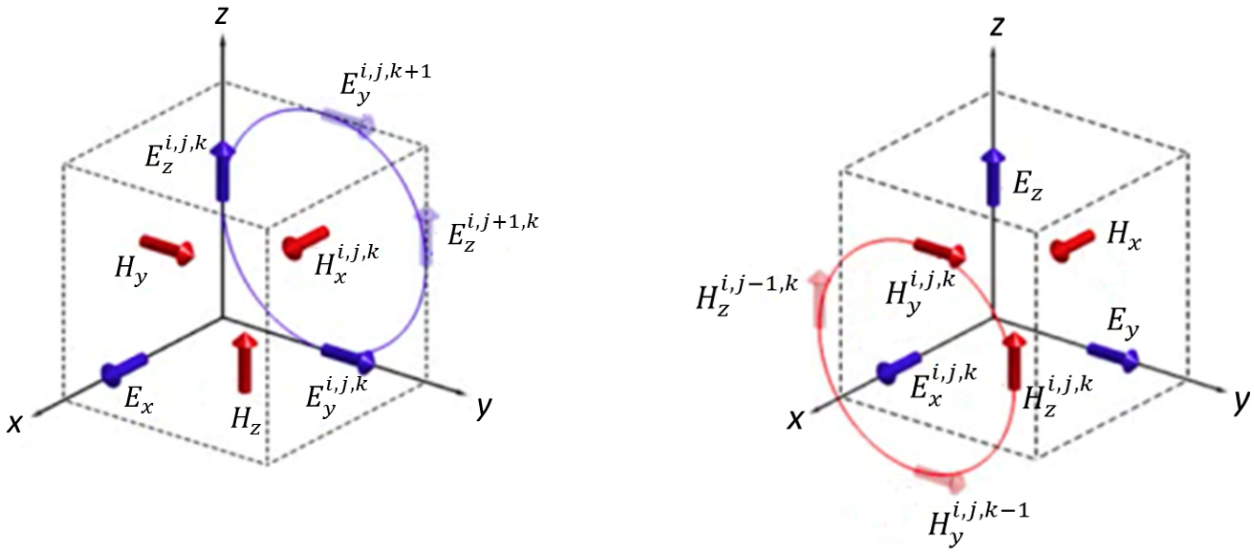

(a) Diagram to visualise discretising H_x field

(b) Diagram to visualise discretising H_x field

Figure 12: Yee grid for H_x and E_x field components

The finite difference equations can then be used to formulate a set of 'update' equations, which can be used to simulate electromagnetic radiation traversing through space and time. The FDTD program initially sets both the electric and magnetic field to zero. A source is introduced in the program in order to generate a non-zero electric and magnetic field. The $\vec{E}$ and $\vec{H}$ fields are updated (based on the update equations) from one another, i.e. the $\vec{E}$ field is updated from the curl of the $\vec{H}$ field, then the $\vec{H}$ is updated from the curl of the $\vec{E}$ field. This process is iterated through time. This mechanism is the basic requirement for generating a simulated electromagnetic field propagating through a grid.

The update equations for the E_x component of the electric field is obtained from Equation 61;

$$E_x^{i,j,k}|_{t+\Delta t} = E_x^{i,j,k}|_t + \frac{\Delta t \cdot c}{\varepsilon_{xx}^{i,j,k}} \left(\frac{H_{n,z}^{i,j,k}|_{t+\Delta t/2} - H_{n,z}^{i,j-1,k}|_{t+\Delta t/2}}{\Delta y} - \frac{H_{n,y}^{i,j,k}|_{t+\Delta t/2} - H_{n,y}^{i,j,k-1}|_{t+\Delta t/2}}{\Delta z} \right) \tag{62}$$

while the update equation for the H_x component of the magnetic field is obtained from Equation 60;

$$H_{n,x}^{i,j,k}|_{t+\Delta t/2} = H_{n,x}^{i,j,k}|_{t-\Delta t/2} - \frac{\Delta t \cdot c}{\mu_{xx}^{i,j,k}} \left(\frac{E_z^{i,j+1,k}|_t - E_z^{i,j,k}|_t}{\Delta y} - \frac{E_y^{i,j,k+1}|_t - E_y^{i,j,k}|_t}{\Delta z} \right) \tag{63}$$

By inserting various object in the FDTD simulation, one can observe how these materials interact with electromagnetic radiation. Through this method, one can predict the optical properties of metasurface devices, such as the reflectance spectra, transmission spectra, phase response for various wavelengths, far-field plots, and electric and magnetic field distributions, to name a few.

Though the Yee grid is very effective in simulating propagating electromagnetic radiation, there are some consequences of having the field components located in physically different directions. One possible issue is that the field components within the same grid cell can reside in different materials. The program accounts for this by creating unique arrays for ε_{xx}, ε_{yy}, and ε_{zz}, which must be constructed separately. The grids also cause wave propagation to occur slightly slower than in real life, a phenomenon known as numerical dispersion. This issue is resolved by decreasing the values of μ_r and ε_r by a factor of γ across the entire grid, i.e. $\mu_r^{'} = \mu_r/\gamma$ and $\varepsilon_r^{'} = \varepsilon_r/\gamma$. Despite these intrinsic consequences that arise due to the composition of the Yee grid, the program accounts for these flaws well, and can produce results to great accuracy, as demonstrated by various works that have compared their FDTD simulated results to their experimental results [2].

Chapter 4

4 Spatially Varied Resonator Geometries

4.1 Introduction

The aim of this section is to optimise the design for a metal-insulator-metal (MIM) beam-steering metasurface device where the resonator elements are long wires, such that the length of the wire is much greater than the width (L>>W). This type of resonator is selected as the optical properties of such a device can be simulated with 2D simulations, where the length of the wire is 'infinitely' large in comparison to the width. This would require significantly less computational time. A device is said to have a MIM structure when the sub-wavelength resonator elements sit upon a dielectric medium, which in turn sits upon a bottom back-reflector. See Figure 14 for the schematic of the MIM beam-steering metasurface structure. The optical response of three different metals are investigated in order to determine which metals are most suitable for the different components of the metasurface. Once the optimum device structure is established, a beam-steering device will be proposed, which will be capable of anomalous reflection when subject to normal incident radiation.

In order for our metasurface structure to be able to achieve anomalous reflection at any desired angle, we must design them such that they are able to 'mould' the reflected wavefronts into arbitrary shapes. As depicted by the generalised Snell's law (Equation 56) in Section 2.2.1, this can be done by controlling the phase of light at every point along the surface of the device. The resonator elements can produce a spatially varied phase response through variations in their geometric dimensions. Section 2.1.5 highlighted the resonant frequency, and therefore resonant wavelength (λ_{res}), of an optical resonator to be a function of its physical dimensions. This resonant wavelength is one of the factors which determines the phase of the reflected light, should the optical resonator element be approximated as a damped-driven harmonic oscillator. This approximation can be made with confidence for Drude-like metals, where the oscillation of the electron system within surface plasmons can be described by simple harmonic motion. Using the relationship, $cos(\phi) = 1/\sqrt{1 + tan(\phi)}$, Equation 52 from Section 2.1.7, which described the phase response of a single resonator element, can be re-written to express ϕ in terms of the incident wavelength (λ), λ_{res}, and the damping coefficient (β). The β term is a factor which inhibits electron oscillation and

accounts for the energy dissipation on the system. We are making the assumption that $\beta/\lambda << 1$, i.e. the damping factor has a smaller effect on the system compared to the driving force of the incident radiation.

$$cos(\phi) = \frac{4\pi^2 c^2(\lambda^2 - \lambda_{res}^2)}{\lambda^2 \cdot \lambda_{res}^2 \sqrt{\frac{16\pi^4 c^4 (\lambda^2 - \lambda_{res}^2)^2}{\lambda^4 \cdot \lambda_{res}^4} + \frac{4\pi^2 c^2 \beta^2}{\lambda^2}}} \tag{64}$$

In order to easily visualise the relationship between the phase response of a single optical resonator, and its resonant wavelength, we can plot ϕ vs λ_{res}, see Figure 13 below. We can see that the phase response of the element increases, in a sigmoid-like manner, as the resonant wavelength increases. The red curve plots the function where all coefficients, constants, and variables are set to 1. The other curves differ in the value of the damping coefficient, Evidently, increasing the value of the damping coefficient 'warps' and 'stretches' out the function around the point of inflection. It seems that resonator materials with a greater damping coefficient will exhibit lower overall phase shifts (phase difference between an element with a low resonant wavelength and that with a high resonant wavelength).

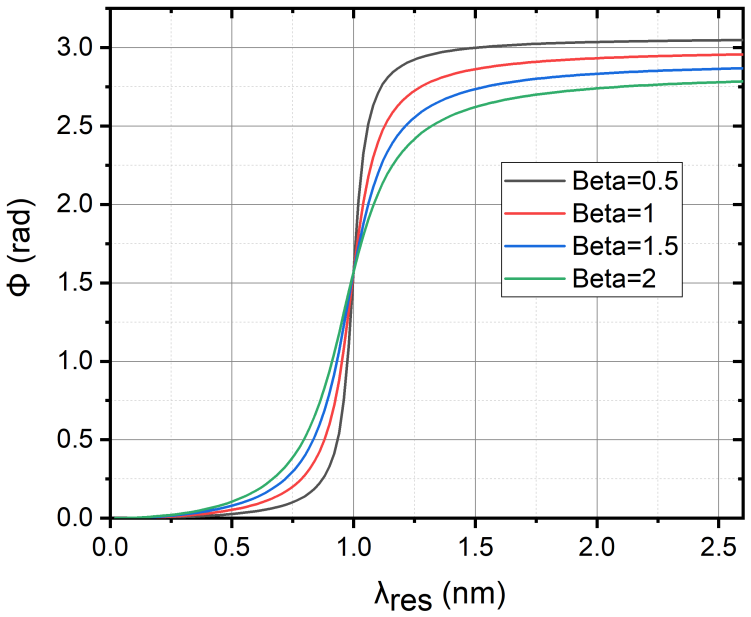

Figure 13: Phase vs resonant wavelength from Equation (64) for various β values.

Classically, the resonance within antenna-like elements is described to occur when the length of

the element is equal to a multiple of the incident wavelength, i.e. $L = const \cdot \lambda$ [67, 68]. However, in the optical frequency regime, this incident wavelength needs to be replaced by a shorter effective resonant wavelength, which is a function of the antenna's geometry, optical properties (ε), and plasma wavelength (λ_p) [67, 69]. Mie theory, describing the absorption within spherical metallic nano-particles, shows that the resonance wavelength is also influenced by the dielectric constant of the material surrounding the resonator element, hereby known as the medium dielectric constant (ε_m) [70, 71, 72]. This is also disclosed by the Gans' equation, which is an extension of the Mie theory and can be applied for ellipsoidal particles [73]. Indeed, a general expression describing the absorption profile for a small metallic particle of arbitrary shape is analogous to the Gan's equation [74]. Many works have demonstrated the linear relationship between λ_{res} and the length of a thin metallic cylindrical resonator element (L) [67, 71]. F. Neubrech *et al.* demonstrated that the resonant behaviour and extinction cross-section of a rectangular nanowire were almost identical to that of perfectly cylindrical nanowires [69]. The devices presented in this work will employ thin, long rectangular nanowires. Analogous to [69], the optical properties of the rectangular nanowires are shown to be similar to that of thin cylindrical elements presented in other works. Note that the linear relationship between antenna length and resonant wavelength is seen when the polarisation of light is such that the electric field lies along the long axis of the antenna element. In the case where the electric field lies along the width of the antenna element, we would expect the resonant wavelength to now increase linearly with increased wire width.

We will compare the optical performances of three different metals; the noble metals gold (Au) and silver (Ag), as well as the base metal aluminium (Al). These metals were selected as they are all well described by the Drude model [35]. Though it is true that Au, Ag, and Al diverge from a pure Drude-like behaviour at roughly 500 nm, 300 nm, and 800 nm incident wavelength, respectively, this is beyond our wavelength range of interest. In order to optimise the design for the MIM metasurface structure, we must explore which combinations of metals achieve the largest overall phase shift across the surface of the device. By investigating the resonant wavelength of each wire element we can get a better understanding of the expected phase response of the resonator.

Though the devices presented in this paper will be capable of achieving relatively large angles of anomalous reflection, it is useful to allow for post-fabrication control of the reflected radiation. This is done by introducing a thin layer of VO_2 in between the two metals of our metasurface. We

will exploit the phase changing properties of VO_2, described in Section 2.3, to be able to switch from anomalous reflection (when the VO_2 is in its monoclinic state) to specular reflection (when the VO_2 is in its rutile state) and *vice versa*. As mentioned in Section 1.1, such post-fabrication switching has been demonstrated by previous works utilising alternative PCMs, such as $Ge_2Sb_2Te_s$ (GST) [22, 27]. However, since the transition temperate for VO_2 is significantly lower than that for GST ($\sim 68°$ as opposed to $\sim 145°$), VO_2 is a far more energy efficient option. VO_2 based structures have been previously utilised for colour tuning and colour switching applications [75], phase modulation [2], polarisation control [76], as well as a dynamically controlled phased array based on a slot nano-antenna design [3].

4.2 Device Design & Simulation Set-up

Figure 14a is a schematic of the cross-sectional area of a single resonator element hoisted by our proposed metasurface device structure. The device contains a 45 nm thick metallic caps, which rests upon a 20 nm layer of VO_2. The dielectric substrate material is a 20 nm thick layer of SiO_2, which is followed by a 100 nm thick metallic back-reflector. A thin layer of Ti (2 nm thick) is used as an adhesive agent between each top metallic wire and VO_2. The period (Δx) of each resonator element is 500 nm. As previously mentioned, the length (L) of the resonator element is such that $L >> W$. The optical properties of this set-up is explored for the various cap materials, i.e. Au, Ag, and Al. The material of the back-reflector will also vary between these three selected metals.

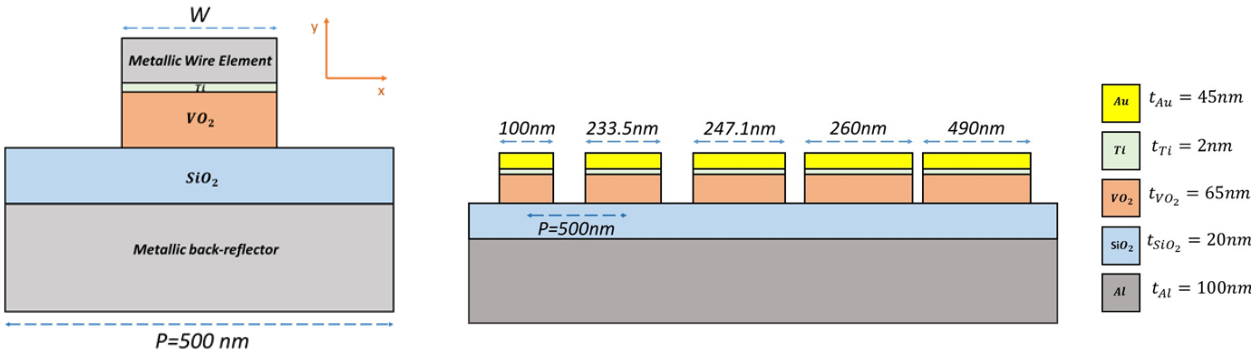

(a) (b)

Figure 14: Schematic of MIM metasurface structure for device with spatially varied resonator elements

(a) Cross-section of a device containing a single resonator element. The material of the top wire element and bottom back-reflector will change between Au, Ag, and Al. (b) Cross-section of the full metasurface structure, containing five resonator elements of different widths.

Figure 14b is a schematic of the cross-sectional area of the full beam-steering device. This device is analogous to that presented in Figure 14a, but will contain five resonator elements, differing in wire length. The length of each consecutive wire gradually increases, and since the period of each resonator remains 500 nm, the separation between each wire decreases. As discussed in Section 2.1.6, the smaller gaps between neighbouring wires will contribute to strong near-field coupling.

When setting our FDTD simulations, a plane wave source is set at normal incidence to the surface of our device structure. The polarisation of light is such that the electric field is parallel to the width (W) of the resonator element (i.e. along the x-direction). When investigating the optical response of structures which exhibit near-field coupling, periodic boundary conditions are applied in the x-direction, while perfectly matched layers (PML) are applied in the y-direction. When investigating the resonant wavelength for a single wire element, PML boundary conditions are applied in both the x and y-directions.

Note that for this specficic device set-up, it is easier to see how a change in the wire width effects the resonant wavelength of the device, when the electric field is along the x-direction. If we were to polarise the light such that the electric field lies along the long axis of the resonator element (along the z-direction), a change in the wire width would cause little change in the aspect ratio (L/W), since $L >> W$, and thus a less obvious change in the resonant wavelength. Although

historically, papers have avoided exploiting the transverse plasmonic resonance due to the lower light intensity it produces [77], this was necessary for a comparative study to explore the suitability of different metals for the various components of the beam-steering device, especially given the long wire structure of our resonator element. This wire structure was selected due to the advantage that it can be investigated using 2D simulations, which is significantly faster than the equivalent 3D simulation. In addition, the macro-scale length of the resonator element would make it far easier to fabricate using common laboratory techniques. However, we compromise the device efficiency in favour for these advantages, which we will discuss in more detail later on.

The material properties for VO_2 were obtained from [78]. The properties for Au, Ag, and Al were obtained from [79], while the properties for Ti were obtained from [80].

4.3 Optical Properties of Different Metals

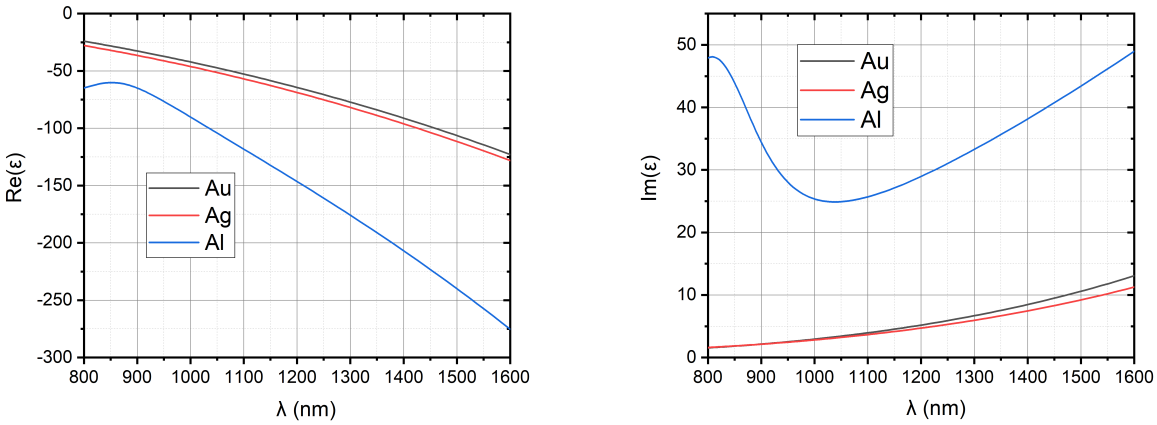

(a) Real permittivity for Au, Ag, and Al

(b) Imaginary permittivity for Au, Ag, and Al

Figure 15: Real and Imaginary permittivity for Au, Ag, and Al

Optical properties obtained from [78]

Figure 15 illustrates the real and imaginary permittivity of the various metals we will be investigating. Evidently, the real permittivity of Al is relatively close to that for Au and Ag at smaller wavelengths. However, as the incident wavelength becomes larger, the real permittivity value diverges further from Au and Ag, with a substantial difference at $\lambda = 1600$ nm. The real component

of the permittivity for Au and Ag is almost the same, with Re(ε) for Au being very slightly higher for all wavelengths in this range.

This gives a good insight into the expected performance of each material. Gans' equation for small ellipsoidal particles, as well as Fuchs' equation for cubic particles [73, 81] suggest that the resonant wavelength decreases with larger |Re(ε)| values. Since |Re(ε)| for Al is larger, we would expect the resonant wavelength for any device hosting an Al top wire to be lower than if the wires were made from Au or Ag, particularly at larger incident wavelengths. Since |Re(ε)| for Au and Ag is almost the same across all incident wavelengths, we would expect the resonant wavelength for devices hosting Au and Ag wires to be almost identical, with that for Au being very slightly higher.

The imaginary component of the permittivity for all materials can be used to infer which material is the most lossy. Ohmic absorption is proportional to the material conductivity $\sigma(\omega)$, which can be related to the permittivity by; Im(ε) = $\frac{\sigma(\omega)}{\varepsilon_o \cdot \omega}$ [33, 36]. Therefore, materials with higher imaginary parts of their permittivity would exhibit higher intrinsic Ohmic losses. Figure 27b depicts Al to be the most lossy material, with Ag as the least lossy (though Im(ε) for Au and Ag are very similar). This would be particularly useful to consider for the top wire element of the device. It is less important to consider the loss which occurs in the bottom back-reflector, as we would expect less penetration of radiation this deep within the structure. Note that Im(ε) is not just useful to describe Ohmic losses within the resonator material, but it also influenced the position of its resonant wavelength. However, the effects of Re(ε) on the resonant wavelength dominates.

4.4 Results & Discussion

4.4.1 Comparison of Various Metallic Cap Material with Au Back-Reflector

We will start our investigation by comparing the optical response of three devices, differing only in the material for the top resonator element (wire). The back-reflector for all devices will be Au. Figure 16a-16c presents the reflectance spectra for devices containing a single Au, Ag, and Al resonator element respectively. This is done for various wire width. Note that since the electric field lies along the x-direction, we see the resonant wavelength redshift with increased wire width. If the polarisation of light was such that the electric field was along the length of the resonator

element (z-direction), we would expect to see a blueshift as the width increases, as this would cause a decrease in the resonator aspect ratio.

The resonant wavelength can be taken as the lowest point of reflection, where the absorption is maximum. The insets of of each plot depicts the relationship between the resonant wavelength and the wire width. As expected, the relationship for all wire materials is linear.

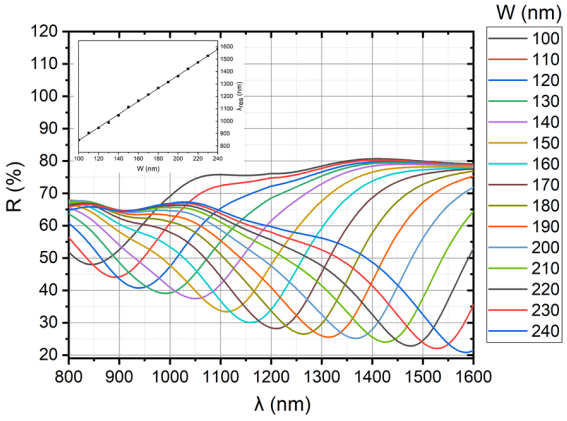

(a) Reflectance spectra for Au wire and Au back-reflector

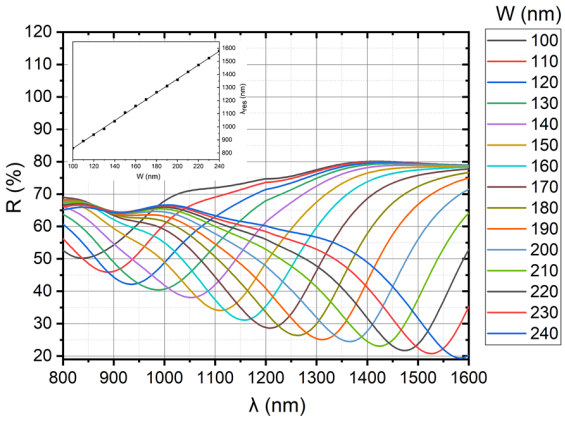

(b) Reflectance spectra for Ag wire and Au back-reflector

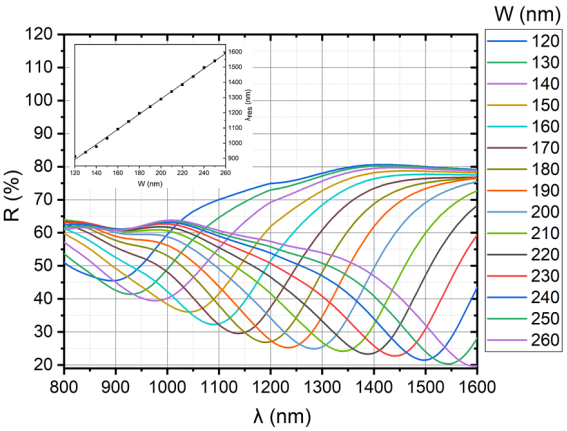

(c) Reflectance spectra for Al wire and Au back-reflector

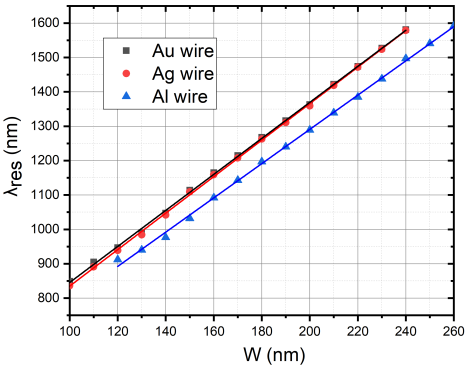

(d) λ_{res} vs L for all wire materials and Au back-reflector

Figure 16: Reflectance spectra and resonant wavelength for all wire materials and Ag back-reflector

Figure 16d provides a direct comparison of λ_{res} vs W for the various metals. As previously discussed, this will give a good indication as to which wire material will provide the largest phase shift across the device structure. Clearly, λ_{res} for Al is lower than that for Au and Ag. The

difference between their resonant wavelengths starts off small, with a $\sim 3\%$ difference at 120 nm wire length, but becomes more substantial as the wire length increases, with a $\sim 5\%$ difference at 240 nm wire length. This results in a lower slope (m) of the linear plot, λ_{res} vs W, for Al than that for Au and Ag.

From Equation 64 and Figure 13, we can see that the phase response of each wire element increases with a greater resonant wavelength. Since there is a linear relationship between λ_{res} and W, we can relate them using the equation of a line; $\lambda_{res} = c + m \cdot W$, where c is the y-intercept. Increasing the value of m would effectively 'stretch' the plot in Figure 13 about the point of inflection along the y-direction. This would result in a greater phase shift (difference between ϕ at a point of low λ_{res} and high λ_{res}). Note here that we are not yet considering the impact that the damping coefficient, β, has upon the shape of the ϕ vs λ_{res} plot. Since the slope of λ_{res} vs W for a device containing an Al wire is significantly lower than that for an Au and Ag wire, we would also expect the overall phase shift between a wire of small length (small λ_{res}) and a wire of large length (large λ_{res}) to be lower than that for Au and Ag.

Since the difference between λ_{res} for Au and Ag is essentially negligible across all wire widths, we would expect the phase shift between Au wires of small and large lengths to be almost identical to that produced by Ag wires. This is not surprising, given the chemical and optical similarities between Au and Ag in the NIR [82]. It is interesting to note that this similarity between Au and Ag is not seen at extremely low wire dimensions, i.e. below 5 nm length [83]. Here, Ag nanowires were found to exhibit resonant peaks, while Au nanowires of the same dimension didn't. This is a result of interband transitions, which are closer to the Fermi energy level in Au than in Ag [84].

Having discussed the impact that λ_{res} has upon the overall phase shift across the surface of the device, we can now look at the influence of β. As discussed in Section 4, and presented in Figure 13, a higher damping coefficient leads to a gentler slope at the point of rapid phase increase, thus resulting in a lower overall phase shift between points of low λ_{res} (small wire width) and high λ_{res} (large wire width). Since $\mathrm{Im}(\varepsilon)$ is related to the loss of the material, which is represented by β, we would expect the most lossy of the three metals to exhibit the highest β value. Section 4.3 depicted Al to have the largest $\mathrm{Im}(\varepsilon)$ across the NIR, and thus the largest β. This reinforces the expectation for a device containing Al wires to produce the lowest phase shift. Since $\mathrm{Im}(\varepsilon)$ for Au and Ag are very similar, their damping coefficients are expected to be virtually the same.

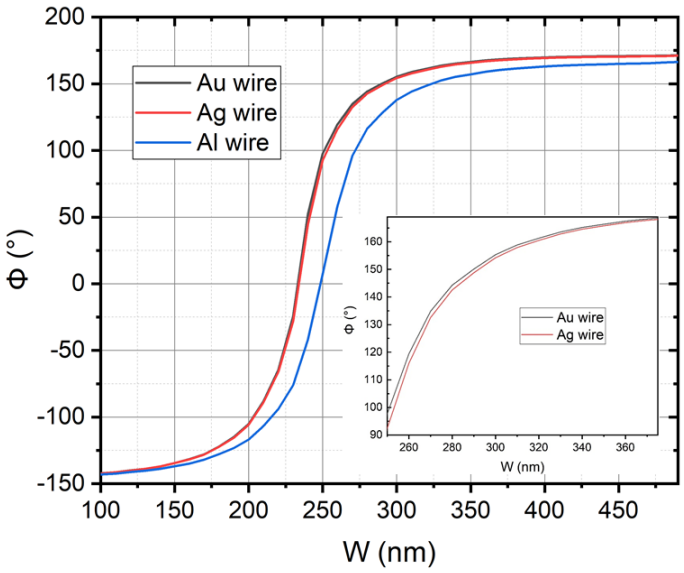

Figure 17: Phase *vs* wire width for all materials with an *Au* back-reflector
Inset shows close-up comparison of *Au* and *Ag* wires

Figure 17 presents the relationship between the phase response and wire width for each resonator material at a representative incident wavelength of 1550 nm. From these plots, we can see which element materials result in the largest phase shift between a wire of small width (100 nm) and a wire of large width (490 nm), see Table 1. These results confirm our expectations for *Al* wires to exhibit the lowest phase shift, and *Au* and *Ag* wires to exhibit the highest. The phase shift for *Au* and *Ag* wires is indeed almost equal, with a negligible difference.

Table 1: Total Phase Shift for Devices Containing *Au* Back-Reflector

Material	Au	*Ag*	*Al*
$\Delta\phi$ (°)	313.7	313.4	309.6

These results present *Au* and *Ag* to be the most suitable materials as the top resonator elements, for devices containing an *Au* back-reflector. Though we suspect changing the material of the metallic back-reflector to have a major impact on the device performance (since the dielectric constant of the medium surrounding the resonator element, ε_m, changes), all devices should consistently depict *Au* and *Ag* as the superior resonator material, regardless of the material of the back-reflector.

4.4.2 Comparison of Various Metallic Cap Material with Ag Back-Reflector

We will analyse exactly how the phase shift achieved by our devices is affected by changing the material of the back-reflector from Au to Ag. Since the optical properties of Au and Ag have been shown to be similar in the wavelength range of interest, we would expect $\Delta\phi$ for these devices to also be similar to the results attained when using an Au back-reflector.

Figure 18a-18c illustrate the reflectance spectra for devices containing a single Au, Ag, and Al resonator element respectively for various wire lengths. Again, the insets of each graph convey the linear relationship between λ_{res} and W for all wire materials. Analogous to Figure 16d, Figure 18d provides a comparison for λ_{res} vs W for the various wire materials. Yet again, the slope (m) for Al is significantly lower than that for Au and Ag. The slope for λ_{res} vs W for Au is again almost identical to that for Ag, depicting both Au and Ag to be the most suitable materials for the resonator element, and Al as the least suitable.

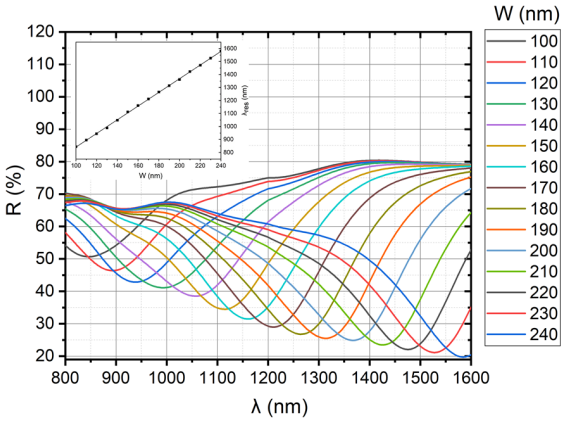

(a) Reflectance spectra for *Au* wire and *Ag* back-reflector

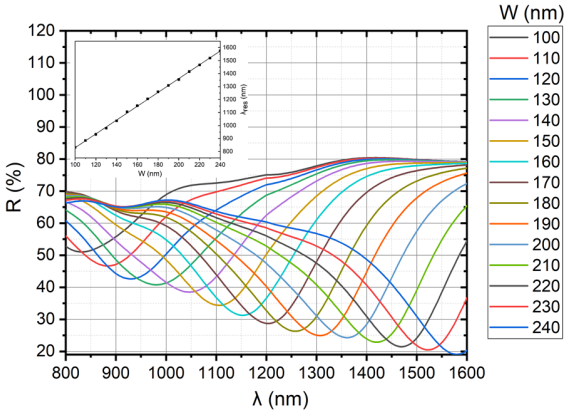

(b) Reflectance spectra for *Ag* wire and *Ag* back-reflector

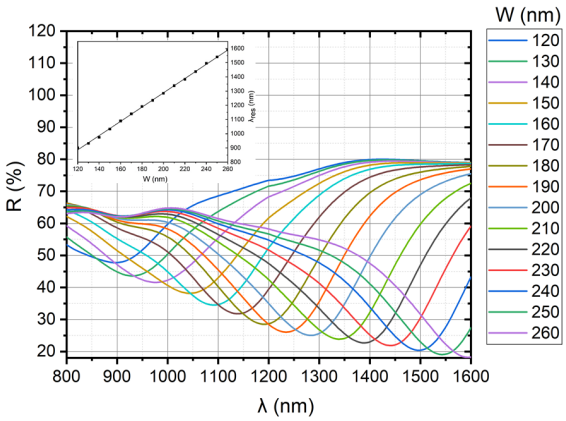

(c) Reflectance spectra for *Al* wire and *Ag* back-reflector

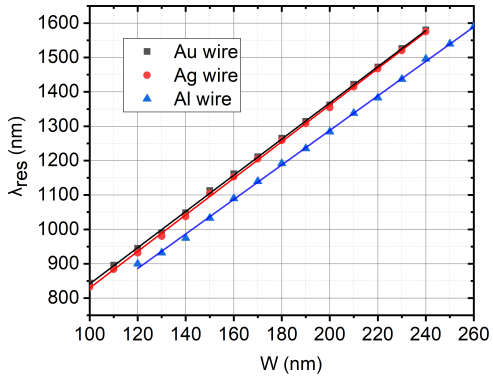

(d) λ_{res} vs L for all wire materials and *Ag* back-reflector

Figure 18: Reflectance spectra and resonant wavelength for all wire materials and *Ag* back-reflector

It is important to note that the resonant wavelengths for all three devices containing an *Ag* back-reflector are lower than those which contain an *Au* back-reflector. This difference is attributed to a change in ε_m. Since the permittivity of *Ag* is slightly lower than that of Au, ε_m slightly decreases when the material of the back-reflector is changed from *Au* to Ag. S. Link *et al.* highlighted the linear relationship between λ_{res} and ε_m [71]. They demonstrated that the position of the resonant wavelength increases as ε_m increased. Since ε_m slightly decreases when replacing the *Au* back-reflector with *Ag* in the NIR, it is no surprise that λ_{res} for all devices containing an *Ag* back-reflector is slightly lower than the corresponding devices containing an *Au* back-reflector.

This decrease in λ_{res} leads to a consequential decrease in ϕ across all wire lengths. However, it is important to note that the decrease in ϕ becomes less and less extreme as the wire width increases. As a result, the overall phase response should be lower for small wire widths, but roughly the same as that for devices containing an Au back-reflector for large wire widths.

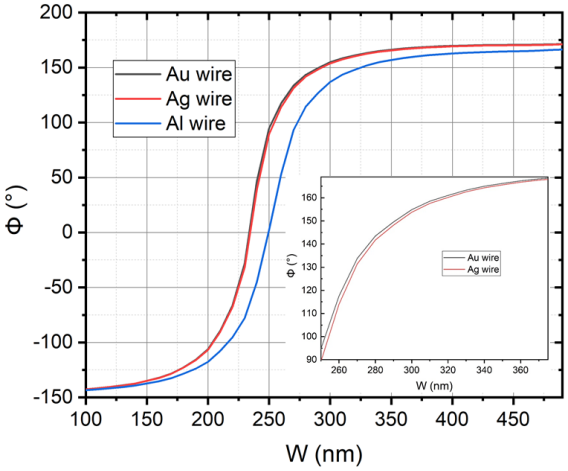

(a) Phase vs wire length for all materials with an Ag back-reflector. Inset shows close-up comparison of Au and Ag wires

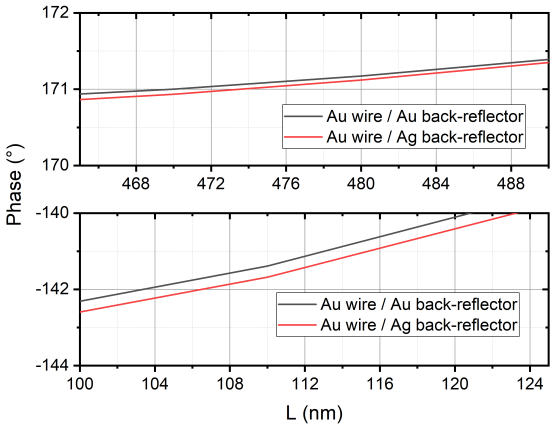

(b) Comparing phase vs wire length for Au wire with an Au and Ag back-reflector.

Figure 19: (a) Phase response vs wire length for all materials with an Ag back-reflector. (b) Comparison of phase vs wire length for device containing Au wire with Au and Ag back-reflector

Figure 19a illustrates the phase response for all resonator materials across the various wire widths for devices containing an Ag back-reflector. The overall phase shifts between a wire of small width (100 nm) and a wire of large width (490 nm) for the various resonator materials is presented in Table 2. Again, $\Delta\phi$ for Au and Ag wires are roughly the same, and considerably higher than that for devices containing Al wires. The results also depict $\Delta\phi$ for the devices containing an Ag back-reflector to be higher than those which contain an Au back-reflector. This is as the phase response for devices containing an Ag back-reflector is significantly lower at small wire widths, but roughly the same as those which contain an Au back-reflector at large wire widths, leading to an overall larger phase shift, as can be seen in Figure 19b. The bottom graph compares the phase response of a device containing Au wires and an Au back-reflector to that which contains Au wires and an Ag back-reflector, at the small wire width scale. The difference between ϕ for the two plots is $\sim 0.2\%$ at a wire width of 100 nm. The top graph compares the phase response of the two devices

in the large wire wdith scale, which highlights the difference in ϕ at a wire width of 490 nm to only be $\sim 0.02\%$, ten times lower than seen at smaller wire widths.

Table 2: Total Phase Shift for Devices Containing *Ag* Back-Reflector

Material	Au	*Ag*	*Al*
$\Delta\phi$ (°)	313.9	313.7	309.8

4.4.3 Comparison of Various Metallic Cap Material with *Al* Back-Reflector

Finally, we will perform the same comparative study, but this time looking at devices which contain an *Al* back-reflector. Figure 20a-20c show the reflectance spectra for devices hoisting a single Au, Ag, and *Al* resonator element. The insets again depict the linear relationship between the wire width and transverse resonant wavelength. Yet again, λ_{res} for a device containing an *Au* wire is almost identical to that containing an *Ag* wire, and considerably higher than that containing an *Al* wire, across all wire widths, as seen in Figure 20d.

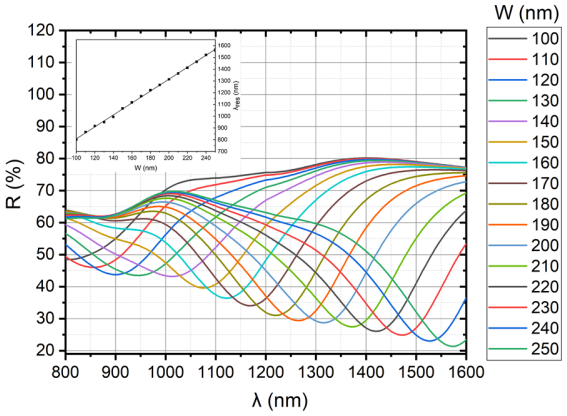

(a) Reflectance spectra for *Au* wire and *Al* back-reflector

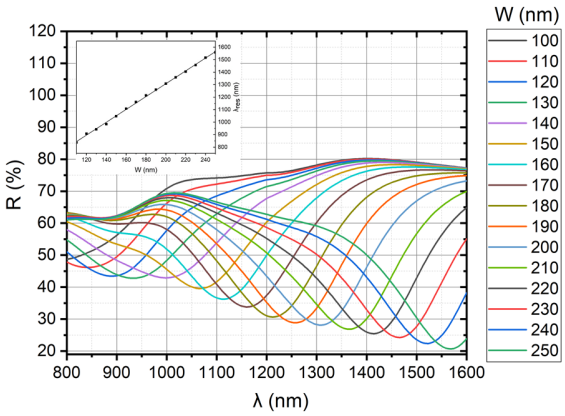

(b) Reflectance spectra for *Ag* wire and *Al* back-reflector

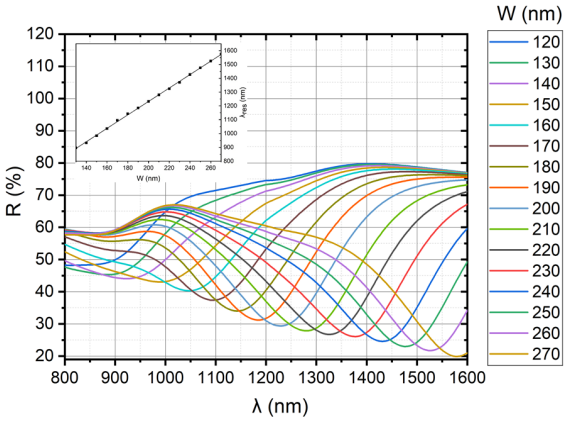

(c) Reflectance spectra for *Al* wire and *Al* back-reflector

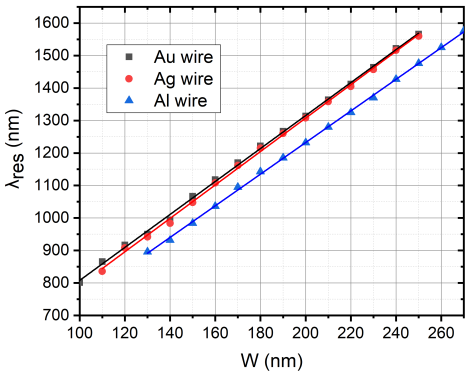

(d) λ_{res} vs L for all wire materials and *Al* back-reflector

Figure 20: Reflectance spectra and resonant wavelength for all wire materials and *Al* back-reflector

Due to this resonant behaviour, *Au* and *Ag* can be considered as the most suitable reflect array metals, while *Al* is found to be the least suitable. Figure 21a and Table 3, which depicts the overall phase shift between a wire width of 100 nm and a wire width of 490 nm, for the three devices containing an *Al* back-reflector, supports these findings. This table also conveys that $\Delta\phi$ for devices containing an *Al* back-reflector is higher than those which contain an *Au* or *Ag* back-reflector (see Table 1 and 2).

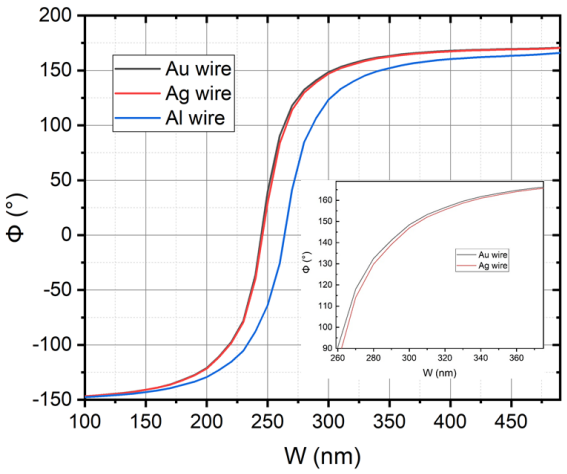

(a) Phase vs wire length for all materials with an *Al* back-reflector. Inset shows close-up comparison of *Au* and *Ag* wires

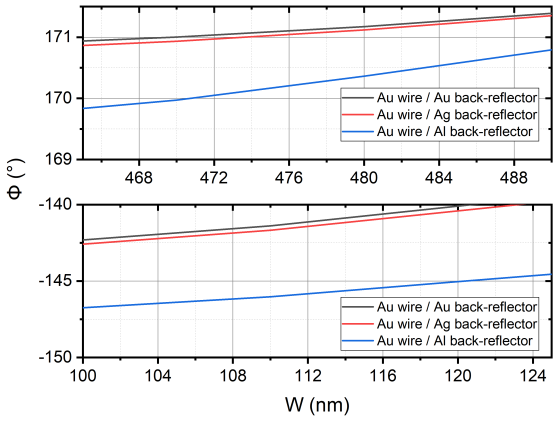

(b) Comparing phase vs wire length for *Au* wire with an Au, Ag, and *Al* back-reflector.

Figure 21: (a) Phase response *vs* wire length for all materials with an *Al* back-reflector. (b) Comparison of phase vs wire length for device containing *Au* wire with Au, Ag, and *Al* back-reflector

The significantly lower permittivity of *Al* compared to that of *Au* and *Ag* suggests that ε_m for devices containing an *Al* back-reflector would be significantly lower than that of an analogous device containing an *Au* or *Ag* back-reflector. However, the difference this ε_m has upon the phase response at high wire widths is minuscule, especially when compared to the difference ε_m makes at lower wire widths. This is illustrated in Figure 21b, which depicts the phase response of three devices. All devices contain an *Au* resonator elements, but differ in the material of the back-reflector. The lower graph shows the difference in the phase response at smaller wire widths, while the upper graph shows the difference in the phase response at larger wire widths. At a wire width of 100 nm, there is a $\sim 3\%$ difference in ϕ between a device containing an *Au* wire and *Al* back-reflector to that which contains an *Au* wire and *Au* back-reflector (see lower graph of Figure 21b). This phase discrepancy is roughly ten times higher than seen at wire widths of 490 nm, where the difference in ϕ between a device containing an *Au* wire and *Al* back-reflector to that which contains an *Au* wire and *Au* back-reflector is $\sim 0.3\%$ (see upper graph of Figure 21b).

Due to its substantially lower permittivity, *Al* can be regarded as the most suitable back-reflector of our MIM beam-steering device. This is as the lower permittivity of *Al* leads to lower ε_m, which

Table 3: Total Phase Shift for Devices Containing *Al* Back-Reflector

Material	Au	*Ag*	*Al*
$\Delta\phi$ (°)	317.5	317.3	313.4

has a considerable influence on ϕ at small wire widths, but little effect at large wire widths.

4.5 Proposed Beam-Steering Device

Now that we have established the most suitable materials as the top resonator element and bottom back-reflector, we can proceed to designing a MIM metasurface beam-steering device. This device will be capable of switching between anomalous reflection and specular reflection due to the phase changing properties of VO_2. Though our findings suggest both Au and Ag to be equally as suitable as the resonator element, we will utilise Au due to its higher melting temperature [85]. The back-reflector material will be Al. Figure 14b illustrates the transverse cross-section of this device set-up.

Figure 22a illustrated the phase response for our device at each wire width, when the VO_2 is in its monoclinic and rutile phase. The device is subject to normal incident radiation, where $\lambda =$ 1550 nm. The overall phase shift when the VO_2 component is in its monoclinic state is $\sim 317.5°$. In contrast, the phase response is roughly constant when the VO_2 is in its rutile state.

We will choose our device to host five resonator elements, differing only in wire width. We need to carefully elaborate over the width of each wire so that our device will exhibit a constant phase shift between each consecutive wire. This will establish a linear phase profile across the device surface, as shown by the black plot in Figure 22b. Each point on the plot represents the position of the centre of each resonator element. The red plot in Figure 22b depicts the near constant phase response across the device surface when the VO_2 is in its rutile state. The wire width and corresponding phase response for each resonator is presented in Table 4.

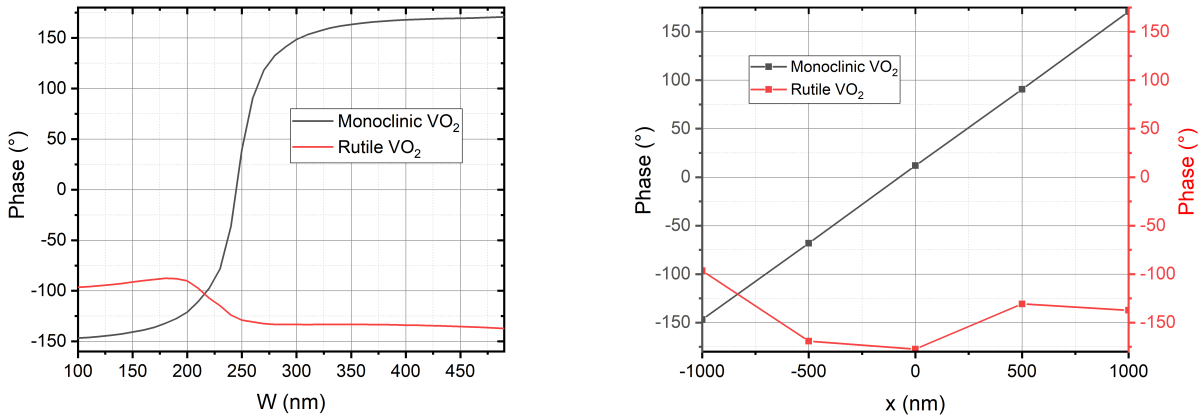

(a) Phase vs wire length for monoclinic and rutile VO_2 (b) Phase vs surface position for monoclinic and rutile VO_2

Figure 22: Phase *vs* wire width and surface position for purposed MIM metasurface beam-steering device.

Table 4: Wire Widths and Corresponding Phase Response for Full Device

Wire Width (nm)	100	233.5	247	260	490
ϕ (°)	-146.7	-68.2	11.9	90.6	170.8

The generalised Snell's law, given by Equation 56, allows us to theoretically predict the angle of anomalous reflection that our device can realise when the VO_2 is in its monoclinic state. The calculation suggests an anomalous reflection angle of $\sim 40°$. Since the phase profile across the surface of the device is roughly constant when VO_2 is in its rutile state, $\Delta\phi$ in Equation 56 is ~ 0, and specular mirror-like reflection is achieved. Therefore, by heating the VO_2 component of the metasurface, one can switch between anomalous and specular reflection. As discussed in Section 2.3, this switching occurs once the transition temperature is reached. The switching is also reversible upon cooling. Works such as [2] have demonstrated the phase switching within sub-wavelength VO_2 wires, of similar dimensions, experimentally using resistive heating.

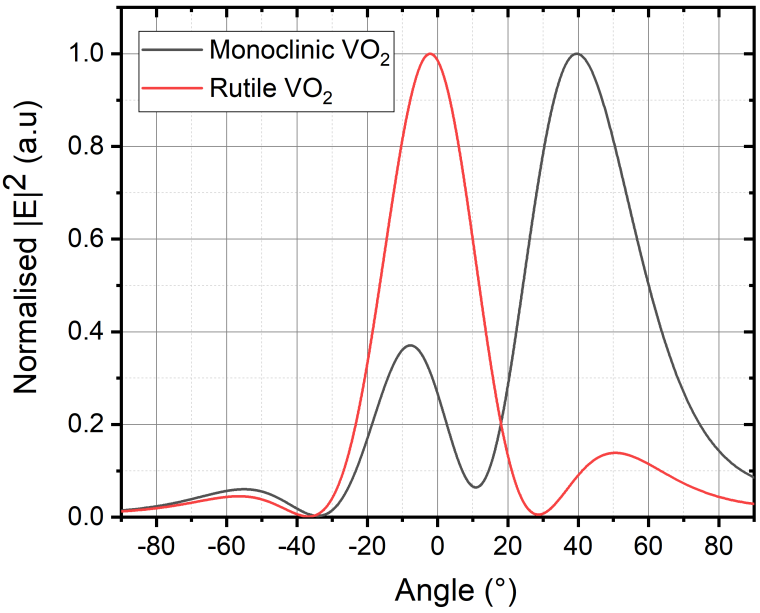

Figure 23: Normalised far-field plots for purposed metasurface device for monoclinic and rutile VO_2

Figure 23 shows the far-field plots of our device set-up to be in good agreement with our theoretical predictions of θ_r for both monoclinic and rutile phases of VO_2.

In order to visualise the penetration depth of radiation within our device, Figure 24 depicts the transverse cross-section of the magnetic field distribution within the metasurface for both monoclinic and rutile phases of VO_2. Both the left and right panels depict the field to be primarily confined within the wire element of the device, with little radiation present within the Al back-reflector. This implies that the back-reflector should have little impact on the efficiency of the proposed device, despite the higher intrinsic Ohmic losses of Al. The figure presents the material of the top reflect-array wire to have a bigger affect on the efficiency of the beam-steering device.

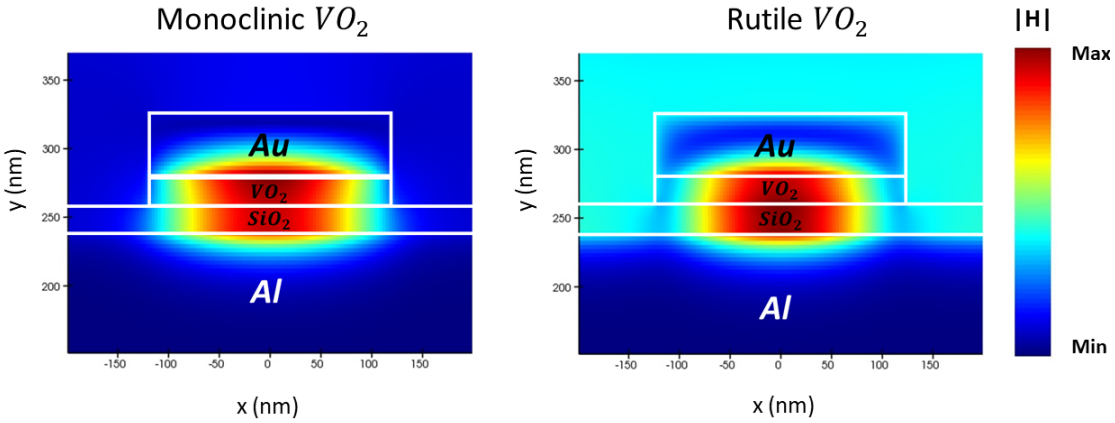

Figure 24: Transverse cross-section of magnetic field-distribution within device containing monoclinic and rutile VO_2

As previously mentioned, since we utilise the transverse surface plasmons of our resonator element, the reflectance of light is relatively low. Evidently, the reflectance continues to decrease as the width of the resonator element increases, regardless of the metallic material used. This will greatly affect the efficiency of our device. We found the deflection efficiency to be $\sim 10\%$. This is defined as the ratio of the intensity of the main lobe (the light present at our maximum anomalous reflection angle) and the sum off all the background intensities [86, 87]. The diffraction efficiency was found to be $\sim 0.1\%$, which is defined as the ratio of of the intensity of the main lope and the total input intensity. This is $10\times$ lower than works such as [88], and $100\times$ lower than that of recent, state-of-the art, geometric plasmonic metasurfacs operating in the visible and NIR regions of the spectra [89].

Although our proposed MIM metasurface beam-steering device can achieve a large, tunable anomalous reflection angle, it is necessary to explore ways in which to improve the deflection and diffraction efficiencies in order for these devices to be useful in practical applications. Works such as [90, 91] have highlighted various ways in which to improve the diffraction efficiency of such devices.

4.6 Conclusion

We have conducted a comparative study on three different Drude-like metals (Au, Ag, and Al), in order to establish which metals are most suitable as the different components of a MIM metasurface beam-steering device which utilises reflect-array elements such that $L >> W$. Our findings depicted

both Au and Ag to be the most suitable reflect-array materials, and Al to be the most suitable back-reflector material. This is assuming the electric field lies along the width of the resonator element.

The investigation highlighted that the relationship between λ_{res} and W for each metallic material provides insight as to which material would lead to the higher overall phase shift across the surface of the beam-steering device. This is connected to the real component of the material's permittivity, $\mathrm{Re}(\varepsilon)$. We also discussed how the intrinsic damping coefficient, β, of the device influences the overall phase shift, which is connected to the imaginary part of the material's permittivity, $\mathrm{Im}(\varepsilon)$. In conclusion, for Drude-like metals, the material of the top reflect-array wire should exhibit a high $\mathrm{Re}(\varepsilon)$ at the wavelength range of interest (to ensure a high slope in the λ_{res} vs W plot), and a low $\mathrm{Im}(\varepsilon)$ (to ensure a low β coefficient). While the electric field lies along the width of the resonator elements, these properties would lead to the optimum conditions when attempting to realise a large phase shift between resonators of small wire widths and resonators of large wire widths. Our study also disclosed the impact that the permittivity of the material surrounding the resonator element (ε_m) has upon the performance of the device. The effective dielectric medium was varied by changing the material of the bottom metallic back-reflector. A lower effective ε_m has been shown to lead to larger phase shifts across the device surface. Therefore, for Drude-like metal, a material with low permittivity is most suitable as the bottom back-reflector of the beam-steering device.

Note that in this study we only attempted to optimise the performance of the device by investigating which metals are most suitable as the top reflect-array elements and bottom back-reflector, but did not look at which material would be most suitable as the dielectric or insulator component of the MIM structure. Using the same argument that we used for the bottom back-reflector, we would expect that a dielectric or insulator material with a lower dielectric constant would lead to better device performance. Note that in this context, better device performance implies a larger overall phase shift across the device surface. We did not focus on optimising device efficiency.

A MIM metasurface beam-steering device was also proposed, using the metals we found to be most suitable as the top resonator element and bottom back-reflector. The PCM VO_2 was used to allow for post-fabrication anomalous-to-specular reflection switching. Our device was able to achieve an anomalous reflection angle of $\sim 40^\circ$ when the VO_2 was in its monoclinic state, and

specular reflection ($\sim 0°$) when the VO_2 was in its rutile state.

The results of this section have demonstrated how a large phase shift, thus a large angle of anomalous reflection, can be achieved by varying the geometry (i.e. width) of the optical resonator elements. The following section will explore alternative ways to realise metasurface beam-steering. The first method will involve adjusting the local medium dielectric constant, ε_m, surrounding each resonator element, while maintaining a constant element geometry. The second and final method will present a device hosting resonator elements which exhibit variations in both their geometric dimensions, as well as their local surrounding environment. The advantages and disadvantages of each type of device are discussed.

Chapter 5

5 Thermally Graded Metasurface

5.1 Introduction

As we have seen, a metasurface can achieve a desired reflection angle through their compositional design and positioning of the optical resonator elements. Snell's generalised law (Equation 56) depicts how this reflection angle is related to the phase shift across the surface of the device. We have demonstrated the relationship between the length of an individual resonator element and its phase response (Section 2.1.5), and proposed a device which exhibits a spatially varying phase due to the spatial variation in wire length. We have also shown that the geometry of the resonator element is not the only factor which influences the behaviour of the surface plasmons within metallic nanowires. The surface plasmon resonance, spectral bandwidth, radiation profile, and efficiency of a resonator element is also determined by the dielectric environment surrounding each element, i.e. the medium dielectric constant introduced in Section 4 (ε_m).

The ability to adjust the dielectric environment post-fabrication enables the tuning of the resonant frequency and phase response of each resonator element. Such capability can be exploited to increase the functionality of typical beam-steering devices. Our previous device, and works such as [22, 27], have demonstrated post-fabrication switching between two discrete points; a predetermined anomalous reflection angle and a specular reflection angle. However, by allowing governance over the dielectric environment of each resonator element, with the ability to continuously tune the optical properties of the dielectric environment, one can create a beam-steering device where the angle of reflection can be continuously tuned in between the anomalous and specular reflection angles. In order to enable the tuning of the optical properties of the dielectric environment, one would need to include an active component within the device (consisting of otherwise passive components). Since VO_2 can offer a considerably large tuning capability at a relatively low transition temperature, we will again use this PCM as the active component within our metasurface beam-steering device. However, it is important to note that such active components can include any material which is susceptible to elastomeric stretching, free carrier effects, and non-linear effects. Other materials besides PCMs, which exhibit intrinsic structural-changing properties in response

to an external stimulus can also be employed, such as liquid crystals [92]. Previously, we have exploited the ultra-fast transition of VO_2 from a monoclinic (low-temperature) to a rutile (high-temperature) structure, but will now take advantage of the intermediate optical properties of VO_2 found in between these two extremities.

The device presented in Section 4.5, which employs spatially varied resonator elements, has disadvantages other than lacking intermediate angle control between the predetermined anomalous reflection and specular reflection angles. One such disadvantage is that the predetermined anomalous reflection angle is only possible in one direction, since the shape of the reflected wavefronts determined by the geometric variation of the resonator elements cannot be easily altered once fabricated. The total attainable angle sweep is thus greatly limited. Furthermore, these type of devices also require increasingly smaller separations between resonators, since the length of the resonator element increases while the period of each wire remains fixed. This can enhance localised near-field coupling within the separation gap between each resonator, as discussed by Section 2.1.6 [33]. This near-field coupling between densely packed resonator elements may lead to digressions from the expected performance of the metasurface device [93], as the phase response of each wire elements is sensitive to the near-field coupling, as well as the resonator geometry and ε_m. In addition, very narrow separation gaps between adjacent resonator elements would lead to greater difficulty during the fabrication process.

The issues that we have stated above, i.e. the unaccounted enhanced near-field coupling and difficulty during device fabrication, are overcome by designing a metasurface structure (labelled as Structure A) which maintains a constant resonator length, while the environment of each individual element is gradually altered in such a way as to achieve a constant optical phase gradient along the device surface. This is accomplished by progressively adjusting the phase of VO_2 underneath each resonator element. Since the wire length doesn't change, the separation between each adjacent element is kept relatively large. Continuously tuning the phase of VO_2 between its monoclinic and rutile states has been demonstrated by [2], where the temperature of wire elements of similar dimensions were controlled via electrical heating. Their work, carried out both theoretically and experimentally, highlights the feasibility of the metasurface designs proposed here. Since we will establish phase control of each individual resonator element, the anomalous reflection angle in Structure A can be continuously modulated in either the + or - direction by reversing the direction

in which the thermal gradient is applied.

Finally, we will also report on a device that utilises both spatially varying resonator elements and variations in the local environment of each wire (labelled as Structure B). A larger phase shift across the device surface is expected by employing both phase modulating mechanisms. Similar to Structure A, a large separation between adjacent resonator elements is maintained to minimise the unpredictable effects of near-field coupling and for ease of fabrication. We will compare the performance of the two proposed devices.

Again, the NIR region of the spectrum is the wavelength range of interest, due to the wide variety of metasurface application in this region of the spectrum (discussed in Section 1.2). We will report on the performance of our devices at an incident wavelength of 1000 nm.

5.2 Lorentz-Lorenz Model

In Section 2.3, we discussed the way in which a single VO_2 crystal undergoes an abrupt transition from a monoclinic (low temperature), to a rutile (high temperature) phase, when the transition temperature or critical strain is reached. The transition was described to be abrupt [94], which is not desirable if we are to utilise VO_2 to try and achieve a continuous change in refractive index across the surface of our devices. A way in which we can get around this issue is by using thin films of VO_2, which consist of numerous nano crystal grains. These nano grains can undergo transitions at different temperatures, effectively resulting in intermediate phases of VO_2, between purely monoclinic and purely rutile states. This was demonstrated by [95]. These finding depict thin-film VO_2 layers as suitable ways in which to gradually alter the optical properties of successive array elements.

In order to simulate data conveying the relationship between the intermediate VO_2 states and the optical properties of the resonator element (including the phase response), one must employ a model which can deduce the permittivity of the monoclinic/rutile mixture. We can apply a Lorentz-Lorenz model to determine the refractive index and extinction coefficient of a material with an arbitrary volume fraction of monoclinic VO_2. This model has been adapted from the effective medium theory for isotropic linear dielectrics [96]. Though VO_2 is not classified as an isotropic material, the model can be safely applied as long as a single polarisation is excited. The application of models, which assume an isotropic media, on VO_2 has been implemented in other

works which also try and exploit the intermediate properties of an insulator-metal mixture to create a significant phase modulation [3, 97].

The formula below can be used to describe the polarisation density (P_{mix}) of composite materials, specifically for an amalgam of two linear dielectrics. In our case, we are looking to get the polarisation density of a mixture of monoclinic (cold) and rutile (hot) VO_2.

$$P_{mix} = \Omega \cdot P_{cold} + (1 - \Omega) \cdot P_{hot} \tag{65}$$

P_{cold} is the polarisation density of monoclinic VO_2,
P_{hot} is the polarisation density of rutile VO_2,
Ω is the volume fraction of monoclinic VO_2.

It is more useful to define the dielectric constant of the mixture. We can relate the polarisation density to the relative permittivity by employing the Clausius-Mossotti relation [98].

$$\frac{\varepsilon_{mix} - 1}{\varepsilon_{mix} + 2} = \Omega \cdot \frac{\varepsilon_{cold} - 1}{\varepsilon_{cold} + 2} + (1 - \Omega) \cdot \frac{\varepsilon_{hot} - 1}{\varepsilon_{hot} + 2} \tag{66}$$

By noting that $\varepsilon = Re(\varepsilon) + i \cdot Im(\varepsilon)$, and re-expressing the permittivity values for monoclinic and rutile VO_2 in terms of their refractive indices and extinction coefficients, i.e. $Re(\varepsilon) = n^2 - k^2$, and $Im(\varepsilon) = 2nk$, Equation 66 can be written as;

$$\varepsilon_{mix} = \frac{2\alpha + 2\beta + 1}{1 - \alpha - \beta} \tag{67}$$

where,

$$\alpha = \Omega \cdot \left(\frac{n_{cold}^2 - k_{cold}^2 + i \cdot 2 \cdot n_{cold} \cdot k_{cold} - 1}{n_{cold}^2 - k_{cold}^2 + i \cdot 2 \cdot n_{cold} \cdot k_{cold} + 2} \right) \tag{68}$$

and,

$$\beta = (1 - \Omega) \cdot \left(\frac{n_{hot}^2 - k_{hot}^2 + i \cdot 2 \cdot n_{hot} \cdot k_{hot} - 1}{n_{hot}^2 - k_{hot}^2 + i \cdot 2 \cdot n_{hot} \cdot k_{hot} + 2} \right) \tag{69}$$

The graph below depicts the refractive index and extinction coefficient for the insulator-metal mixture with various volume fractions of monoclinic VO_2. As expected, these values lie between those for the extreme phases of VO_2, i.e. volume fractions of 0.0 and 1.0. Evidently, the refractive index increases with increased volume fraction of monoclinic VO_2, with an approximate 60.76% increase between purely rutile (0.0) and purely monoclinic (1.0) VO_2 at a wavelength of 1000 nm. Conversely, the extinction coefficient decreases with increased volume fraction of monoclinic VO_2,

with an approximate 33.97% decrease between monoclinic and rutile VO_2 phases. This trend is in good agreement with works such as [3, 97].

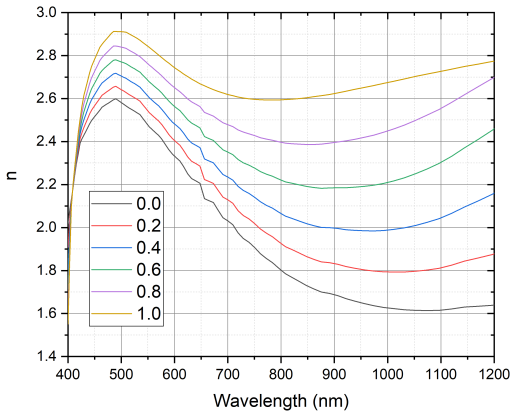

(a) n vs λ for various monoclinic phase fractions

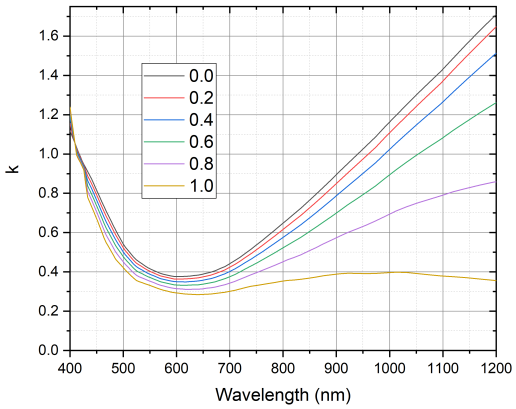

(b) k vs λ for various monoclinic phase fractions

Figure 25: Refractive index and extinction coefficient for various volume fractions of monoclinic VO_2

One can easily relate the changes in n and k values for various volume fractions of VO_2 to its temperature. Works such as [99] have explored the relationship between temperature and the volume fraction of rutile VO_2, which can easily be converted to depict the relationship between temperature and monoclinic phase content. In their case the VO_2 film was 80 nm thick, deposited over an alumina substrate. The graph conveys a roughly linear relationship between temperature and monoclinic phase fraction between $\approx$ 336 K and 342 K, see Figure 26a. By combining the information from Figure 25 and that from Figure 26a, we can see that there is a relatively large change in optical properties over a small temperature difference, see Figure 26b. Using this information, it is possible to experimentally fabricate a metasurface device which requires resistive heating to alter the refractive index and extinction coefficient of consecutive array elements. Figure 26 highlights the potential to achieve relatively large changes in optical properties over a small temperature gradient.

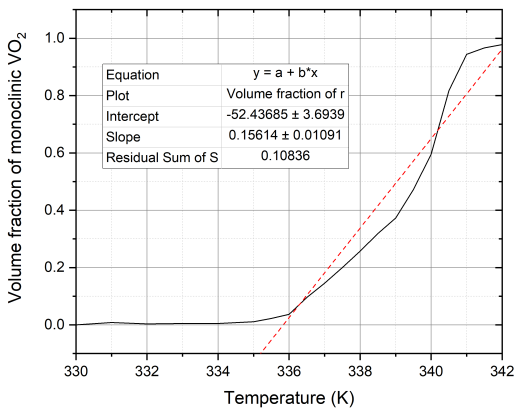

(a) Volume fraction of monoclinic VO_2 vs Temperature (K)

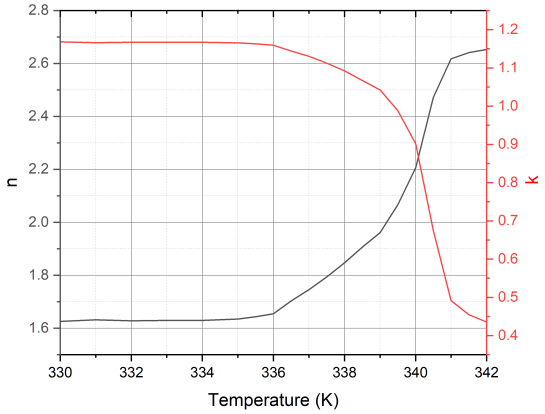

(b) n and k vs Temperature (k) at λ=1000 nm

Figure adapted from [99]

Figure 26: Temperature dependence on monoclinic phase fraction, and refractive index and extinction coefficient at λ=1000 nm

5.3 Device Design & Simulation Set-up

Figure 27a depicts a schematic of the transverse cross-section of a unit cell of Structure A. The diagram conveys a 100 nm thick Au back-reflector, a 20 nm thick planar layer of SiO_2, followed by a 65 nm thick VO_2 wire with a 45 nm thick Ag metal cap. The VO_2 and Ag cap have a length of 200 nm. The period of the unit cell is 400 nm, giving a wire separation of 200 nm.

The transverse cross-section of Structure B is presented in Figure 27b. The device is analogous to that of Structure A, but with variations in the length and separation of the array elements. The lengths of these resonator elements are 100 nm, 140 nm, 170 nm, and 200 nm. By limiting the wire length to 200 nm, the separation between adjacent elements remains large, i.e. above 200 nm.

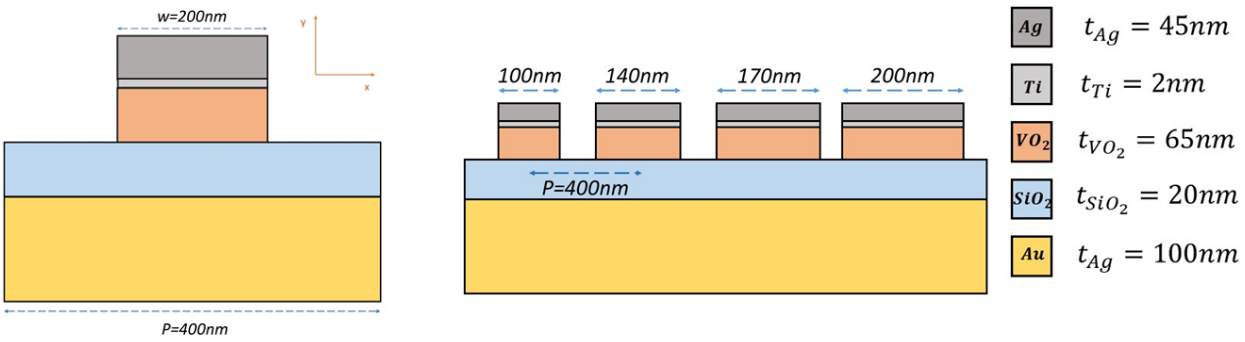

(a) (b)

Figure 27: Transverse cross-section of Structure A and Structure B

Similar to the beam-steering device proposed in Section 4.5, both Structure A and B are simulated using FDTD. Periodic boundary conditions are applied in the x-direction, while perfectly matched layers (PML) boundary conditions are applied in the y-direction. The device is illuminated by a plane wave source at normal incidence to the device surface. The polarisation of light was such that the electric field was parallel to the length of each resonator element.

Again, the optical properties of VO_2 were obtained from [78]. The dielectric permittivity of intermediate phases of VO_2 were interpolated using a Lorentz-Lorenz model, given by Equation 66. The optical properties of Au, Ag, and SiO_2 were obtained from [79], while the properties of Ti were obtained from [80].

Though the devices proposed our theoretical, similar devices have been fabricated using well established fabrication techniques, as demonstrated by [2]. The major differences between the proposed device in Figure 27 and the device fabricated in [2] is that the material of the top metallic cap is Ag rather than Au, the material of the substrate underneath the VO_2 wire is SiO_2 rather than Al_2O_3, the width of the array elements are 200 nm rather than 210 nm, and the thickness of the Ag and VO_2 array elements are 45 nm and 65 nm respectively, rather than 40 nm each.

5.4 Results & Discussion

5.4.1 Thermal Gradient: Structure A

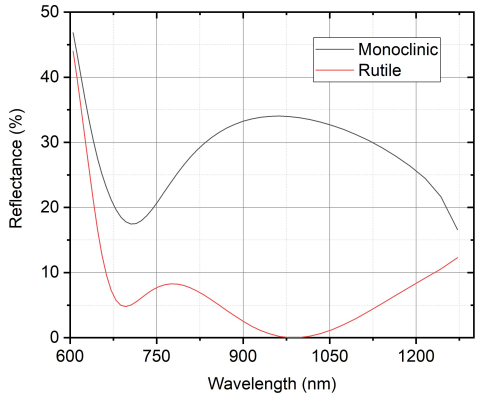

(a) Reflectance spectra of purely monoclinic and rutile VO_2

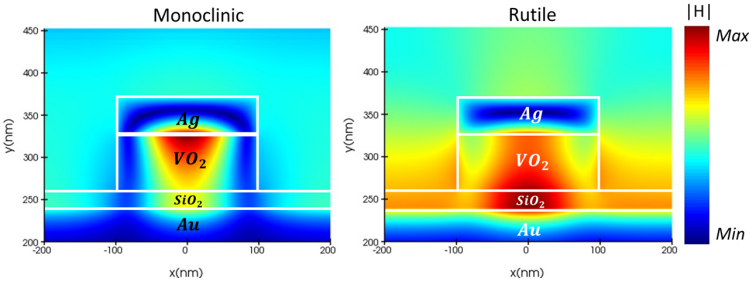

(b) Magnitude of magnetic field distribution within device

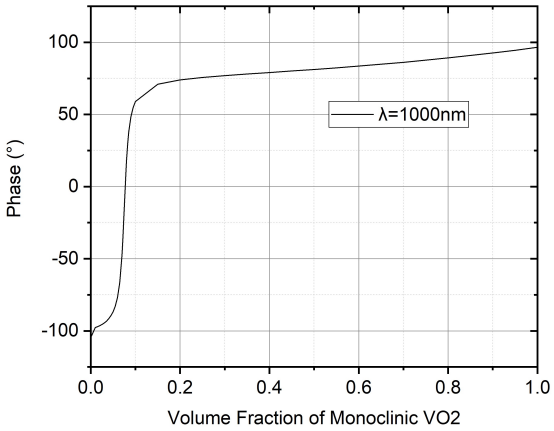

(c) Phase vs volume fraction of monoclinic VO_2

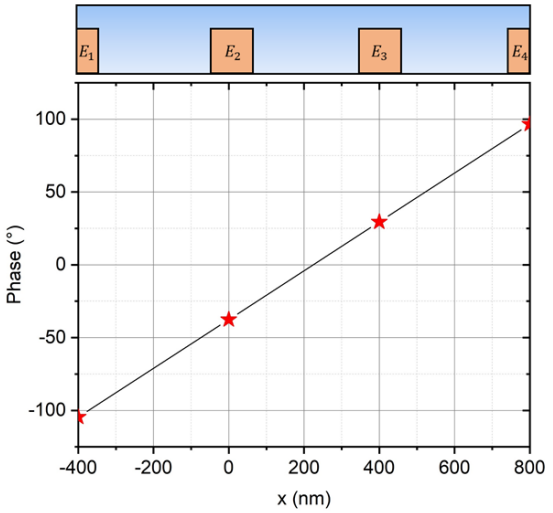

(d) Phase vs position along device surface, volume fraction of VO_2 of each element presented in Table (5)

Figure 28: Performance and analysis of Structure A

Figure 28a illustrates a large difference in reflectance between the monoclinic and rutile states of VO_2. The difference in reflectance between monoclinic and rutile VO_2 remains high across a wide wavelength range, and at $\lambda = 1000$ nm, is as high as 33%. This substantial drop in reflectance is

a consequence of the deeper penetration depth in rutile VO_2, since it behaves as a metal, where the radiation is subject to higher Ohmic losses [23]. Figure 28b is a transverse cross-section of the magnetic field distribution within the device. The left panel of Figure 28b depicts the magnetic field to be primarily confined within the VO_2 element when it is in the monoclinic state. Since the VO_2 behaves as an insulator in this state, the effective dielectric thickness (due to the VO_2 and SiO_2) is increased. However, once the VO_2 transitions to its rutile state, the SiO_2 becomes the only contributor for the dielectric thickness, and the magnetic field is confined lower within the resonator element, see the right panel of Figure 28b. Figure 28a and Figure 28b clearly shows the considerable impact changing the phase of VO_2 has upon device performance. This is due to the substantial difference in optical properties between monoclinic and rutile VO_2, as shown by Figure 25.

Figure 28c illustrates the phase response of our device at each volume fraction of monoclinic VO_2. We can see a maximum phase shift of $\sim 201^\circ$ at $\lambda = 1000$ nm, between elements consisting of purely monoclinic (volume fraction of 1.0) and rutile (volume fraction of 0.0) phases of VO_2. This continuous phase modulation enables control over the shape of the reflected wavefronts, and therefore the angle of reflection. We can choose our device to host four resonator elements, where the volume fraction of monoclinic VO_2 within each element is such that a constant phase gradient is established along the surface of the device, see Figure 28d. The selected volume fractions of monoclinic VO_2 for each resonator element is presented in Table 5. Using the generalised Snell's law, we expect this set-up to be able to achieve an anomalous reflection angle of $\pm 27^\circ$.

Table 5: Properties of Optical Elements in Structure A

Element	1	2	3	4
Volume Fraction	0.0	0.07	0.08	1.0
$\phi\,(^\circ)$	-104.6	-37.6	29.5	96.6

The results are in good agreement with our far-field plots, depicted by Figure 29. Configuration 1 describes the device performance where the leftmost resonator element contains purely rutile VO_2, while the rightmost element contains purely monoclinic VO_2. The volume fractions of the intermediate elements are presented in Table 5. The angle of reflection supports the theoretical calculations provided by the generalised Snell's law. Configuration 2 presents the angle of reflection

where the opposite thermal gradient is applied, which can be easily done by reversing the direction the heat is applied. Both device configurations depict the overall angle sweep to be $\sim 54°$.

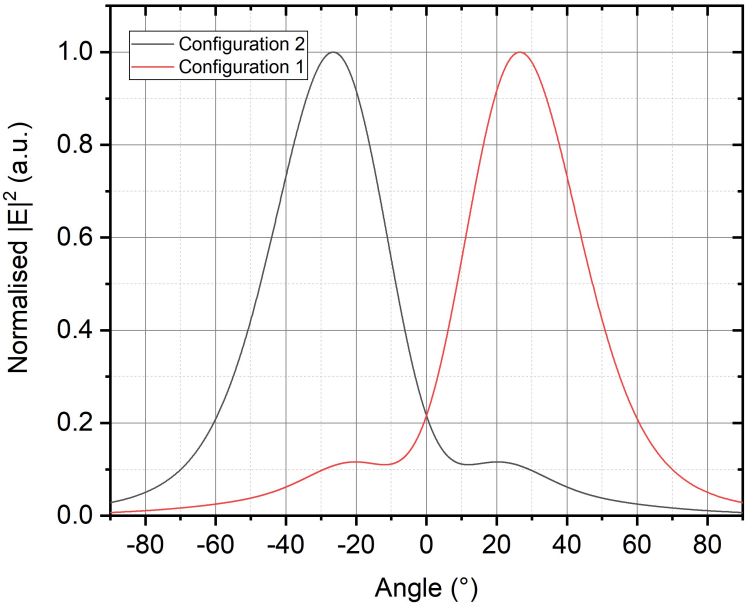

Figure 29: Far-field angular plot of reflected radiation for Structure A

Though the device is capable of a very impressive angle sweep, it is evident from Table 5 that Structure A requires very specific conditions to realise the predetermined anomalous reflection angle of 27°. For example, the phase of VO_2 within the second array element is analogous to that of the third. From Figure 26a, we can see their phase difference requires a temperature difference of $\sim 0.03\%$. This would be particularly difficult to do experimentally, especially considering the sub-wavelength dimensions of the resonator elements. These complications arise from the very steep increase in phase as the volume fraction of monoclinic VO_2 increases from 0.0 to roughly 0.5, see Figure 28c. It is possible for our device to avoid operating in this region in Figure 28c, however, this would greatly diminish the maximum anomalous reflection angle. We will show however, that Structure B does not require such hyper-specific, and impractical conditions.

Another disadvantage of such a device is again the deflection and diffraction efficiencies. In particular, the diffraction efficiency is expected to be extremely low given that most of the VO_2 wire elements are close to the rutile phase. Figure 28a highlights that the reflectance of VO_2 in the

rutile phase is extremely low, particularly at an incident wavelength of 1000 nm (where R(%) ~ 0). Analogous to the device proposed in Section 4.5, the deflection efficiency of Structure A is $\sim 10\%$. However, the diffraction efficiency is significantly lower at $\sim 0.003\%$.

5.4.2 Spatially Varying Resonator Elements &Thermal Gradient: Structure B

Now we will combine the effects of spatially varying the element geometry to that of the phase gradient. Figure 30a and Figure 30b convey the relationship between the width of each wire element, the volume fraction of monoclinic VO_2 within each element, and the phase of reflected light. Evidently, the phase of the reflected light increases with increased wire width due to the higher resonant wavelength present in these wider resonator elements (discussed in Section 4). We can also see that as the VO_2 approaches a pure monoclinic state, the phase shift between small and large wire widths becomes more extreme, before eventually tapering off. The phase shift between a wire width of 100 nm and 200 nm where all elements contain purely monoclinic VO_2 (volume fraction of 1.0) is $\sim 226°$. In contrast, the phase is relatively constant between wires of small and large widths when each element contains purely rutile VO_2 (volume fraction 0.0). The maximum phase shift of 226°, achieved using spatial variations in resonator widths, can be improved by adding a thermal gradient. A phase shift of 239° can be realised by employing a thermal gradient such that the element of width 100 nm contains purely rutile VO_2 and the element of width 200 nm contains purely monoclinic VO_2.

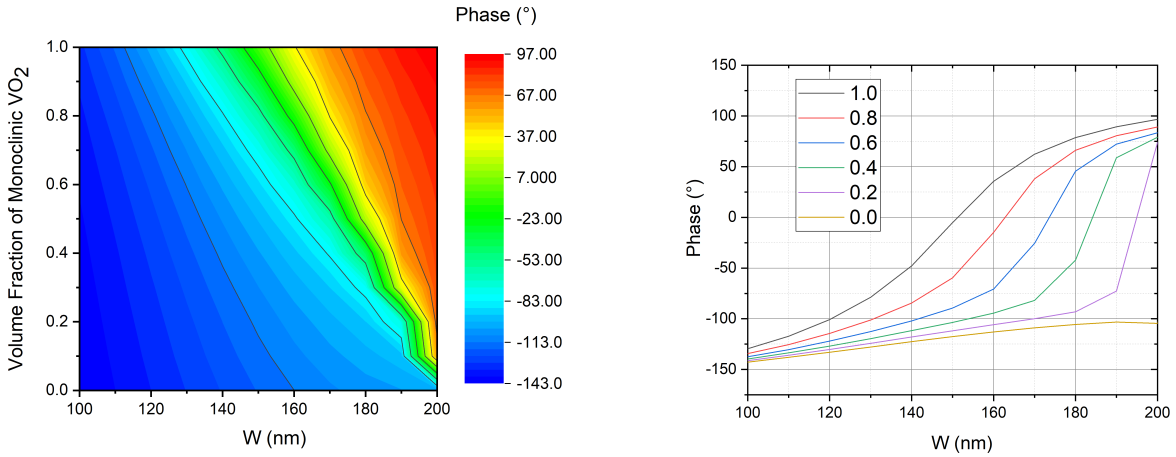

(a) Phase vs volume fraction of monoclinic VO_2 and resonator width

(b) Phase vs resonator width for various volume fractions of monoclinic VO_2

Figure 30: Performance and analysis of Structure B

The characteristic thermal hysteresis loop associated with VO_2 as it transitions between its monoclinic and rutile phases is highlighted clearly by Figure 30b. Evidently, the width of the hysteresis loop increases as the volume fraction of monoclinic VO_2 approaches 0.0, due to the more extreme permutation in lattice structure as the VO_2 approaches its transition temperature.

Again, the device will contain four resonator elements, with the length and volume fraction of monoclinic VO_2 within each element elaborately chosen such that the phase gradient across the device surface is constant, see Figure 31. Table 6 below illustrates the necessary properties of each resonator element. Since the phase shift between each neighbouring resonator element is $\sim 79.8°$, the total angle of anomalous reflection is expected to be $\sim 33°$ from the generalised Snell's law. This means that by combing the effects of spatially varied array geometries and spatial variations in the environment surrounding the resonator element, our device can realise a larger anomalous reflection angle in one direction compared to that which only utilises a thermal gradient, and no variations in resonator geometry. However, since this maximum anomalous reflection angle is only achievable in one direction, the total angle sweep is lower than that of Structure A.

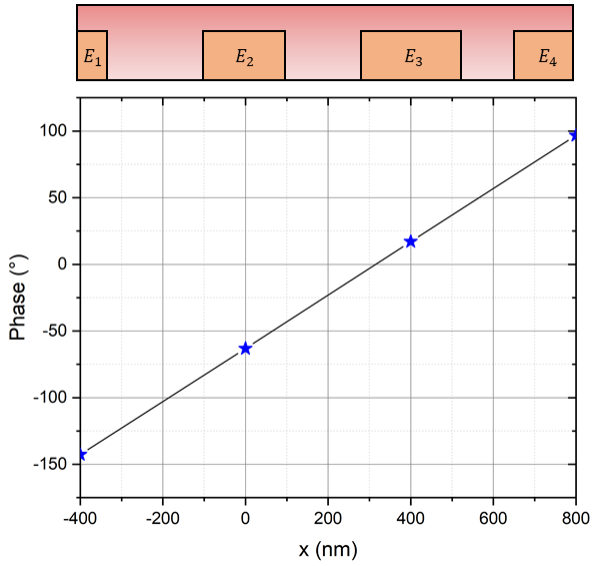

Figure 31: Phase vs position along device surface for Structure B

Volume fraction of VO_2 and wire width presented in Table 6

Table 6: Properties of Optical Elements in Structure B

Element	1	2	3	4
Volume Fraction	0.0	0.9	0.7	1.0
Width (nm)	100	140	170	200
$\phi\,(^\circ)$	-142.7	-63.2	17.0	96.6

Again, our far-field plots support our calculations for the expected angle of anomalous reflection, see Figure 32. Here, configuration 1 presents the performance of the device where each element contains purely rutile VO_2. Since the phase response is roughly constant across all wire widths, the angle of reflection is $\sim 0^\circ$ (specular reflection). It is important to note that this angle is not *exactly* zero, since the phase response is not *exactly* constant. In configuration 2, each resonator element contains varying volume fractions of monoclinic VO_2 so as to achieve the constant phase gradient depicted in Figure 31.

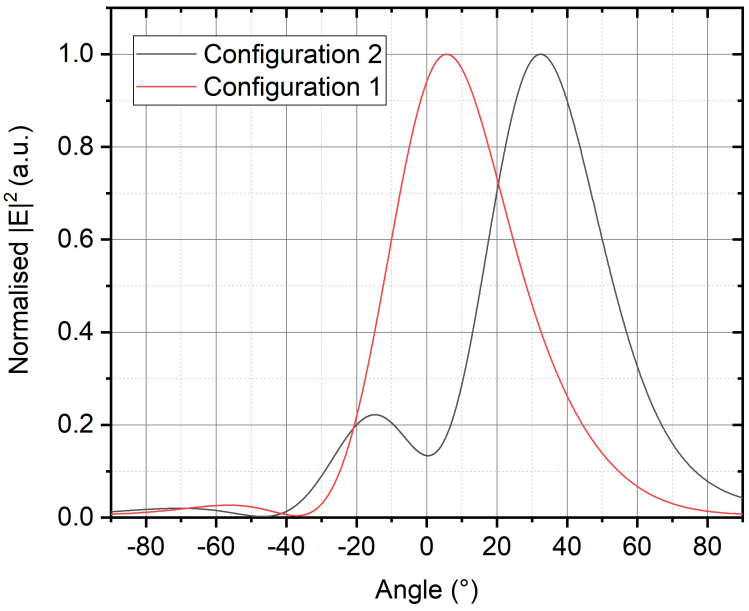

Figure 32: Far-field angular plot of reflected radiation for Structure B

Although we have established in Section 4, and through Figure 30 that a relatively large anomalous reflection angle can be achieved when only utilising spatially varied resonator elements, particularly when each element incorporates purely monoclinic VO_2, the inclusion of the thermal gradient allows for better control over the shape of the reflected wavefronts. By establishing control over the temperature of each resonator element, the reflected light can be directed at an angle between $\sim 0°$ (specular reflection) and $\sim 33°$ (anomalous reflection). This intermediate angle control is not possible when only utilising resonator elements of varied geometries.

Although the maximum angle sweep achieved by Structure B is lower than that of Structure A, it is important to note that the device does not require such fine temperature control for each resonator element, see Table 6.

Similar to Structure A, the deflection efficiency was found to be $\sim 10\%$. The diffraction efficiency was found to be $\sim 0.02\%$, which is higher than that of Structure A, but still significantly lower than that of the device proposed in Section 4.5, and the state-of-the art.

5.5 Conclusion

In summary, two different metasurface beam-steering devices were proposed, each employing a phase change material (VO_2) to allow for continuous tuning of the angle of reflection post-fabrication. The first device, Structure A, which only utilises a thermal phase gradient, can achieve an anomalous reflection angle of $\pm 27^\circ$ at a wavelength of 1000 nm at normal incidence. Intermediate angle control can be realised due to the fine tuning of the optical properties of VO_2, resulting in an overall angle sweep of $\sim 54^\circ$. As this device does not rely on spatially varying the width of each resonator element to achieve a large phase shift, the separation between each element can be relatively large. This helps thermally isolate individual resonator elements from the neighbouring elements, and allows for ease of fabrication. However, Structure A does require very specific conditions to operate that may be difficult to realise in practice. An alternative, hybrid device is thus proposed (Structure B) which incorporates some of the advantages of Structure A, while overcoming its practical limitations.

Structure B employs both spatially varying resonator geometries, as well as a thermal gradient. This type of device exhibits many advantages to devices which only make use of just one of these phase-modulating effects. A device like Structure B can produce a larger anomalous reflection angle, while still maintaining a large separation gap between adjacent resonator elements, compared to that of a device which only employs spatially varying resonator geometries. It also allows for continuous dynamic control over the reflected radiation. A device which does not use a thermal gradient will only exhibit a fixed anomalous reflection angle, or at best, switch discretely between anomalous and specular reflection, as shown by Section 4 and works such as [22, 27]. Although a device like Structure B can also achieve an anomalous reflection angle greater than that which only employs a thermal gradient, such as Structure A, the overall angle sweep is lower since the maximum anomalous reflection angle can only be realised in one direction.

Both Structure A and B highlight the potential for dynamic manipulation of incident radiation using VO_2 based metasurfaces in the NIR.

Chapter 6

6 Conclusions

6.1 Summary of Results

In Section 4 we demonstrated the way in which metasurfaces hosting resonator elements, with spatially varied array geometries, can be used to control the phase of scattered radiation at every point along the device surface. This local phase control was shown to govern the angle of reflected radiation, in accordance with Snell's generalised law. The inclusion of the PCM VO_2 enabled dynamic control over the reflected radiation post-fabrication, i.e. the device proposed in Section 4.5 is theoretically capable of switching between a pre-determined anomalous reflection angle ($\sim 40°$) and a specular reflection angle ($\sim 0°$) at an incident wavelength of 1550 nm. Our metasurface thus behaved as a beam-steering device, capable of a near maximum phase modulation. The metasurface employed a MIM structure. Through an investigative study between three popular Drude-like metals (Au, Ag, and Al), the superior material of the top resonator element was determined to be either Au or Ag (though are device utilised Au), while the superior material of the back-reflector was found to be Al. This specific combination of metals was found to realise the largest overall phase shift across the device surface. Though our resonator elements were rectangular, with the width much smaller than the length, the general conclusions of this section is expected to apply for other resonator geometries, such as elongated ellipsoidal elements, as long as the appropriate polarisation of light is applied.

Though the device proposed in Section 4.5 demonstrated an impressive phase shift, and thus a large anomalous reflection angle, the overall angle sweep was limited as the anomalous refection could only be achieved in one direction. Section 5 presented alternative approaches to local phase control along the device surface. The device described by Section 5.4.1 does not exploit the effects of varying the geometry of the resonator elements, but rather varies the local environment surrounding each element. This can be achieved by controlling the temperature of the VO_2 component underneath each metallic resonator, which provides control over the refractive index and extinction coefficient of the VO_2. By enabling governance over the local medium dielectric constant (ε_m) surrounding each resonator element, the local phase response of each element can

be modified post-fabrication, allowing for the device to be able to achieve anomalous reflection in either direction. The advantages and disadvantages of such a device are discussed. To the best of our knowledge, the device proposed in Section 5.4.1 was therefore capable of achieving one of the largest angle sweeps to date ($\sim 54^\circ$) at an incident wavelength of 1000 nm, by only employing a thermal phase gradient.

A device which employed both changes in the local environment surrounding each resonator element and variations in the element geometry was also proposed in Section 5.4.2. This device had advantages over that described in Section 4.5, such as intermediate angle control between the anomalous reflection angle ($\sim 33^\circ$) and specular reflection angle ($\sim 0^\circ$) also at an incident wavelength of 1000 nm, as opposed to just anomalous-to-specular reflection switching. This device also has the potential to overcome some of the practical issues associated with the device proposed in Section 5.4.1. However, the overall angle sweep was still much lower compared to that achieved by such a device which only employs a thermal gradient due to the inability to realise the maximum anomalous reflection angle in both directions. However, since the operation of this device is more feasible compared to that of Structure A, we believe such a device to have the greatest potential as a plasmonic metasurface beam-steering device.

6.2 Future of Plasmonic Metasurfaces

Though plasmonic metasurfaces can be used to realise impressive phase modulation, and therefore large anomalous reflection angles, they do not make for perfect beam-steering devices. This is due to the intrinsic Ohmic losses associated with metals. These Ohmic losses would decrease the fraction of radiation reflected from the device, lowering the efficiency. This efficiency degradation becomes more extreme at lower incident wavelengths, making these type of beam-steering devices less useful at optical frequencies [100]. Indeed, until recently, the efficiency of plasmonic metasurfaces operating in the visible and NIR regions of the spectra never exceeded that of 10%.

Works such as [21] have employed low-loss, high-permittivity dielectric materials as the optical resonator element for a beam-steering device which enables control over the propagation path of transmitted light. The device they presented was also capable of realising a near perfect phase modulation when subject to normal incident light at 633 nm, while exhibiting little loss. Since the fraction of transmitted radiation remained high across the device surface, the device efficiency was

$\sim$ 80%. Their work suggested that the use of low-loss dielectrics is the future for beam-steering metasurfaces hosting sub-wavelength optical resonators.

Though the efficiency of plasmonic metasurfaces remains lower than that recorded for devices which utilise low-loss dielectric resonator elements, there have been considerable advancements in recent years which highlight the potential for the efficiency of plasmonic metasurfaces to rival that of dielectric metasurfaces. Works such as [89] have come up with innovative ways in which to improve the transmission efficiency of plasmonic metasurfaces in the visible wavelength region to 42.3%, an over 400% increase from that previously recorded. Amongst other things, they employed simple techniques to improve device efficiency, such as introducing an air gap between the metallic resonator element and the surrounding media, which worked to prevent metallic absorption.

As previously discussed, the devices presented in Section 4 and 5 exhibit even lower efficiencies than typical plasmonic reflect-array metasurfaces. This is due to the fact that the devices here exploit the transverse surface plasmon resonance of the array element (electric field is parallel to the width of the resonator element), which leads to a lower light intensity. However, works such as [77] have highlighted the potential for the efficiency of these type of devices to compete with that of devices which make use of the longitudinal surface plasmon resonance (electric field is parallel to the length of the resonator element).

In conclusion, the refinement and enhancement of metasurfaces hosting nano-scale resonator elements is a worthwhile investment due to the potential for these type of devices to be applied to a wide range of fields, such as beam-steering, phase modulation, amplitude control, polarisation manipulation, nanoscale-resolution imaging, optical communication networks, sensing, and much more. Although the intrinsic losses displayed by plasmonic metasurfaces presents complications for such applications, there is great capacity to improve the performance of such devices, making this field of research fruitful and invaluable.

References

[1] F. Venneri, S. Costanzo, G. Di Massa, Tunable Reflectarray Cell for Wide Angle Beam-Steering Radar Applications, Journal of Electrical and Computer Engineering 2013 (2013) 325746. doi:10.1155/2013/325746.
URL https://doi.org/10.1155/2013/325746

[2] Y. Kim, P. C. Wu, R. Sokhoyan, K. Mauser, R. Glaudell, G. Kafaie Shirmanesh, H. A. Atwater, Phase Modulation with Electrically Tunable Vanadium Dioxide Phase-Change Metasurfaces, Nano Letters (2019). doi:10.1021/acs.nanolett.9b01246.

[3] G. Kaplan, K. Aydin, J. Scheuer, Dynamically controlled plasmonic nano-antenna phased array utilizing vanadium dioxide [Invited], Optical Materials Express (2015). doi:10.1364/ome.5.002513.

[4] M. C. Sherrott, P. W. Hon, K. T. Fountaine, J. C. Garcia, S. M. Ponti, V. W. Brar, L. A. Sweatlock, H. A. Atwater, Experimental Demonstration of >230° Phase Modulation in Gate-Tunable Graphene-Gold Reconfigurable Mid-Infrared Metasurfaces, Nano Letters (2017). doi:10.1021/acs.nanolett.7b00359.

[5] D. C. Zografopoulos, G. Sinatkas, E. Lotfi, L. A. Shahada, M. A. Swillam, E. E. Kriezis, R. Beccherelli, Amplitude modulation in infrared metamaterial absorbers based on electro-optically tunable conducting oxides, Applied Physics A: Materials Science and Processing (2018). doi:10.1007/s00339-017-1506-0.

[6] A. Arbabi, Y. Horie, M. Bagheri, A. Faraon, Dielectric metasurfaces for complete control of phase and polarization with subwavelength spatial resolution and high transmission, Nature Nanotechnology 10 (11) (2015) 937–943. doi:10.1038/nnano.2015.186.
URL https://doi.org/10.1038/nnano.2015.186

[7] L.-J. Black, Y. Wang, C. H. de Groot, A. Arbouet, O. L. Muskens, Optimal Polarization Conversion in Coupled Dimer Plasmonic Nanoantennas for Metasurfaces, ACS Nano 8 (6) (2014) 6390–6399. doi:10.1021/nn501889s.
URL https://doi.org/10.1021/nn501889s

[8] P. Genevet, F. Capasso, Holographic optical metasurfaces: Areviewof current progress, Reports on Progress in Physics (2015). doi:10.1088/0034-4885/78/2/024401.

[9] J. Scheuer, Metasurfaces-based holography and beam shaping: Engineering the phase profile of light (2017). doi:10.1515/nanoph-2016-0109.

[10] J. K. Doylend, M. J. R. Heck, J. T. Bovington, J. D. Peters, L. A. Coldren, J. E. Bowers, Two-dimensional free-space beam steering with an optical phased array on silicon-on-insulator, Optics Express (2011). doi:10.1364/oe.19.021595.

[11] L. Zou, M. Cryan, M. Klemm, Phase change material based tunable reflectarray for free-space optical inter/intra chip interconnects, Optics Express (2014). doi:10.1364/oe.22.024142.

[12] Z. Wei, Y. Cao, X. Su, Z. Gong, Y. Long, H. Li, Highly efficient beam steering with a transparent metasurface, Optics Express (2013). doi:10.1364/oe.21.010739.

[13] C. T. M. Wu, J. S. Sun, Microwave metamaterials-based ultrafast detecting scheme for automotive radars, Microwave and Optical Technology Letters (2015). doi:10.1002/mop.29079.

[14] F. Aieta, P. Genevet, M. A. Kats, N. Yu, R. Blanchard, Z. Gaburro, F. Capasso, Aberration-free ultrathin flat lenses and axicons at telecom wavelengths based on plasmonic metasurfaces, Nano Letters (2012). doi:10.1021/nl302516v.

[15] F. Aieta, P. Genevet, M. Kats, F. Capasso, Aberrations of flat lenses and aplanatic metasurfaces, Optics Express (2013). doi:10.1364/oe.21.031530.

[16] D. Hasan, C. P. Ho, C. Lee, Realization of Fractal-Inspired Thermoresponsive Quasi-3D Plasmonic Metasurfaces with EOT-Like Transmission for Volumetric and Multispectral Detection in the Mid-IR Region, ACS Omega (2016). doi:10.1021/acsomega.6b00201.

[17] H. Chu, Q. Li, B. Liu, J. Luo, S. Sun, Z. H. Hang, L. Zhou, Y. Lai, A hybrid invisibility cloak based on integration of transparent metasurfaces and zero-index materials, Light: Science and Applications (2018). doi:10.1038/s41377-018-0052-7.

[18] G.-Y. Lee, J. Sung, B. Lee, Metasurface optics for imaging applications, MRS Bulletin 45 (3) (2020) 202–209. doi:10.1557/mrs.2020.64.

[19] N. Yu, F. Capasso, Flat optics with designer metasurfaces (2014). doi:10.1038/nmat3839.

[20] M. Chen, M. Kim, A. M. Wong, G. V. Eleftheriades, Huygens' metasurfaces from microwaves to optics: A review (2018). doi:10.1515/nanoph-2017-0117.

[21] L. Zou, W. Withayachumnankul, C. M. Shah, A. Mitchell, M. Bhaskaran, S. Sriram, C. Fumeaux, Dielectric resonator nanoantennas at visible frequencies, Optics Express (2013). doi:10.1364/oe.21.001344.

[22] C. R. de Galarreta, A. M. Alexeev, Y. Y. Au, M. Lopez-Garcia, M. Klemm, M. Cryan, J. Bertolotti, C. D. Wright, Nonvolatile Reconfigurable Phase-Change Metadevices for Beam Steering in the Near Infrared, Advanced Functional Materials (2018). doi:10.1002/adfm.201704993.

[23] L. Novotny, B. Hecht, Principles of nano-optics, 2009. doi:10.1017/CBO9780511794193.

[24] N. Yu, P. Genevet, M. A. Kats, F. Aieta, J. P. Tetienne, F. Capasso, Z. Gaburro, Light propagation with phase discontinuities: Generalized laws of reflection and refraction, Science (2011). doi:10.1126/science.1210713.

[25] M. A. Kats, R. Blanchard, P. Genevet, F. Capasso, Nanometre optical coatings based on strong interference effects in highly absorbing media, Nature Materials (2013). doi:10.1038/nmat3443.

[26] M. A. Kats, D. Sharma, J. Lin, P. Genevet, R. Blanchard, Z. Yang, M. M. Qazilbash, D. N. Basov, S. Ramanathan, F. Capasso, Ultra-thin perfect absorber employing a tunable phase change material, Applied Physics Letters (2012). doi:10.1063/1.4767646.

[27] C. R. De Galarreta, A. Alexeev, J. Bertolotti, C. D. Wright, Phase-Change Metasurfaces for Dyamic Beam Steering and Beam Shaping in the Infrared, in: Proceedings - IEEE International Symposium on Circuits and Systems, 2018. doi:10.1109/ISCAS.2018.8351784.

[28] Z. Yang, C. Ko, S. Ramanathan, Oxide electronics utilizing ultrafast metal-insulator transitions, Annual Review of Materials Research (2011). doi:10.1146/annurev-matsci-062910-100347.

[29] P. Guo, A. M. Sarangan, I. Agha, A review of germanium-antimony-telluride phase change materials for non-volatile memories and optical modulators (2019). doi:10.3390/app9030530.

[30] A. M. Taibi, A. Durant, C. Lacoste, D. T. Binnie, L. L. Spada, Metasurfaces for sensing and medical diagnostics, in: 2019 IEEE International Conference on RFID Technology and Applications, RFID-TA 2019, 2019. doi:10.1109/RFID-TA.2019.8892231.

[31] L. La Spada, Metasurfaces for advanced sensing and diagnostics, Sensors (Switzerland) (2019). doi:10.3390/s19020355.

[32] H. Chen, Z. Lin, L. Mo, T. Wu, C. Tan, Near-infrared spectroscopy as a diagnostic tool for distinguishing between normal and malignant colorectal tissues, BioMed Research International (2015). doi:10.1155/2015/472197.

[33] P. Biagioni, J. S. Huang, B. Hecht, Nanoantennas for visible and infrared radiation (2012). arXiv:1103.1568, doi:10.1088/0034-4885/75/2/024402.

[34] S. A. Maier, Plasmonics: Fundamentals and applications, 2007. doi:10.1007/0-387-37825-1.

[35] M. Iwanaga, Plasmonic resonators: Fundamentals, advances, and applications, 2016. doi:10.4032/9789814745079.

[36] S. Wentworth, M. Baginski, D. Faircloth, S. Rao, L. Riggs, Calculating Effective Skin Depth for Thin Conductive Sheets, 2006. doi:10.1109/aps.2006.1711728.

[37] S. Hu, M. Khater, R. Salas-Montiel, E. Kratschmer, S. Engelmann, W. M. Green, S. M. Weiss, Experimental realization of deep-subwavelength confinement in dielectric optical resonators, Science Advances (2018). arXiv:1707.04672, doi:10.1126/sciadv.aat2355.

[38] S. A. Maier, Surface plasmon polaritons at metal/insulator interfaces, in: Plasmonics: Fundamentals and Applications, Springer, 2007, pp. 21–37.

[39] S. Maier, Plasmonics: Fundamentals And Applications, 2007, p. 245.

[40] G. Goubau, Surface waves and their application to transmission lines, Journal of Applied Physics (1950). doi:10.1063/1.1699553.

[41] W. Rechberger, A. Hohenau, A. Leitner, J. R. Krenn, B. Lamprecht, F. R. Aussenegg, Optical properties of two interacting gold nanoparticles, Optics Communications (2003). doi:10.1016/S0030-4018(03)01357-9.

[42] L. Novotny, Strong coupling, energy splitting, and level crossings: A classical perspective, American Journal of Physics (2010). doi:10.1119/1.3471177.

[43] R. P. Feynman, R. B. Leighton, M. L. Sands, Optics: The Principle of Least Time, in: The Feynman Lectures on Physics volume 1, 1963. doi:10.1119/1.1972241.

[44] S. D. Brorson, H. A. Haus, Diffraction gratings and geometrical optics, Journal of the Optical Society of America B (1988). doi:10.1364/josab.5.000247.

[45] F. J. Morin, Oxides which show a metal-to-insulator transition at the neel temperature, Physical Review Letters (1959). doi:10.1103/PhysRevLett.3.34.

[46] M. F. Becker, A. B. Buckman, R. M. Walser, T. Lépine, P. Georges, A. Brun, Femtosecond laser excitation of the semiconductor-metal phase transition in VO2, Applied Physics Letters (1994). doi:10.1063/1.112974.

[47] S. Lysenko, A. Rúa, V. Vikhnin, F. Fernández, H. Liu, Insulator-to-metal phase transition and recovery processes in V O2 thin films after femtosecond laser excitation, Physical Review B - Condensed Matter and Materials Physics (2007). doi:10.1103/PhysRevB.76.035104.

[48] A. Cavalleri, C. Tóth, C. W. Siders, J. A. Squier, F. Ráksi, P. Forget, J. C. Kieffer, Femtosecond structural dynamics in vo2 during an ultrafast solid-solid phase transition, Physical Review Letters (2001). doi:10.1103/PhysRevLett.87.237401.

[49] M. Hada, K. Okimura, J. Matsuo, Characterization of structural dynamics of VO2 thin film on c-Al2O3 using in-air time-resolved x-ray diffraction, Physical Review B - Condensed Matter and Materials Physics (2010). doi:10.1103/PhysRevB.82.153401.

[50] C. Kübler, H. Ehrke, R. Huber, R. Lopez, A. Halabica, R. F. Haglund, A. Leitenstorfer, Coherent structural dynamics and electronic correlations during an ultrafast insulator-to-metal phase transition in VO2, Physical Review Letters (2007). doi:10.1103/PhysRevLett.99.116401.

[51] M. Nakajima, N. Takubo, Z. Hiroi, Y. Ueda, T. Suemoto, Photoinduced metallic state in v O2 proved by the terahertz pump-probe spectroscopy, Applied Physics Letters (2008). doi:10.1063/1.2830664.

[52] I. P. Radu, B. Govoreanu, S. Mertens, X. Shi, M. Cantoro, M. Schaekers, M. Jurczak, S. De Gendt, A. Stesmans, J. A. Kittl, M. Heyns, K. Martens, Switching mechanism in two-terminal vanadium dioxide devices, Nanotechnology (2015). doi:10.1088/0957-4484/26/16/165202.

[53] N. F. Mott, Metal-insulator transition (1968). doi:10.1103/RevModPhys.40.677.

[54] N. F. Mott, The basis of the electron theory of metals, with special reference to the transition metals, Proceedings of the Physical Society. Section A (1949). doi:10.1088/0370-1298/62/7/303.

[55] G. Grüner, The dynamics of charge-density waves, Reviews of Modern Physics (1988). doi:10.1103/RevModPhys.60.1129.

[56] A. Zylbersztejn, N. F. Mott, Metal-insulator transition in vanadium dioxide, Physical Review B (1975). doi:10.1103/PhysRevB.11.4383.

[57] R. M. Wentzcovitch, W. W. Schulz, P. B. Allen, VO2: Peierls or Mott-Hubbard? A view from band theory, Physical Review Letters (1994). doi:10.1103/PhysRevLett.72.3389.

[58] A. Cavalleri, T. Dekorsy, H. H. Chong, J. C. Kieffer, R. W. Schoenlein, Evidence for a structurally-driven insulator-to-metal transition in VO 2: A view from the ultrafast timescale [2], Physical Review B - Condensed Matter and Materials Physics (2004). doi:10.1103/PhysRevB.70.161102.

[59] J. Cao, E. Ertekin, V. Srinivasan, W. Fan, S. Huang, H. Zheng, J. W. Yim, D. R. Khanal, D. F. Ogletree, J. C. Grossman, J. Wu, Strain engineering and one-dimensional organization

of metal-insulator domains in single-crystal vanadium dioxide beams, Nature Nanotechnology (2009). doi:10.1038/nnano.2009.266.

[60] Y. Tokura, Correlated-electron physics in transition-metal oxides, Physics Today (2003). doi:10.1063/1.1603080.

[61] K. Miyano, T. Tanaka, Y. Tomioka, Y. Tokura, Photoinduced insulator-to-metal transition in a perovskite Manganite, Physical Review Letters (1997). doi:10.1103/PhysRevLett.78.4257.

[62] A. Asamitsu, Y. Tomioka, H. Kuwahara, Y. Tokura, Current switching of resistive states in magnetoresistive manganites, Nature (1997). doi:10.1038/40363.

[63] K. S. Yee, Numerical Solution of Initial Boundary Value Problems Involving Maxwell's Equations in Isotropic Media (1966). doi:10.1109/TAP.1966.1138693.

[64] A. Taflove, M. E. Brodwin, Numerical Solution of Steady-State Electromagnetic Scattering Problems Using the Time-Dependent Maxwell's Equations, IEEE Transactions on Microwave Theory and Techniques (1975). doi:10.1109/TMTT.1975.1128640.

[65] A. Taflove, M. E. Brodwin, Computation of the Electromagnetic Fields and Induced Temperatures Within a Model of the Microwave-Irradiated Human Eye, IEEE Transactions on Microwave Theory and Techniques (1975). doi:10.1109/TMTT.1975.1128708.

[66] J. Schneider, Understanding the finite-difference time-domain method, 2011.

[67] L. Novotny, Effective wavelength scaling for optical antennas, Physical Review Letters (2007). doi:10.1103/PhysRevLett.98.266802.

[68] T. A. Milligan, Modern Antenna Design, 2005. doi:10.1002/0471720615.

[69] F. Neubrech, D. Weber, R. Lovrincic, A. Pucci, M. Lopes, T. Toury, M. L. De La Chapelle, Resonances of individual lithographic gold nanowires in the infrared, Applied Physics Letters (2008). doi:10.1063/1.3003870.

[70] G. Mie, Contributions to the optics of turbid media, particularly of colloidal metal solutions (1908). doi:10.1002/andp.19083300302.

[71] S. Link, M. B. Mohamed, M. A. El-Sayed, Simulation of the optical absorption spectra of gold nanorods as a function of their aspect ratio and the effect of the medium dielectric constant (1999). doi:10.1021/jp990183f.

[72] G. C. Papavassiliou, Optical properties of small inorganic and organic metal particles (1979). doi:10.1016/0079-6786(79)90001-3.

[73] R. Gans, Über die Form ultramikroskopischer Silberteilchen, Annalen der Physik (1915). doi:10.1002/andp.19153521006.

[74] R. Fuchs, S. H. Liu, Sum rule for the polarizability of small particles (1976). doi:10.1103/PhysRevB.14.5521.

[75] K. Wilson, C. A. Marocico, A. L. Bradley, Dynamic structural colour using vanadium dioxide thin films, Journal of Physics D: Applied Physics (2018). doi:10.1088/1361-6463/aac47c.

[76] P. Cormier, T. V. Son, J. Thibodeau, A. Doucet, V. V. Truong, A. Haché, Vanadium dioxide as a material to control light polarization in the visible and near infrared, Optics Communications (2017). doi:10.1016/j.optcom.2016.07.070.

[77] Q. Ruan, C. Fang, R. Jiang, H. Jia, Y. Lai, J. Wang, H. Q. Lin, Highly enhanced transverse plasmon resonance and tunable double Fano resonances in gold@titania nanorods, Nanoscale (2016). doi:10.1039/c5nr08521g.

[78] T. V. Son, K. Zongo, C. Ba, G. Beydaghyan, A. Haché, Pure optical phase control with vanadium dioxide thin films, Optics Communications (2014). doi:10.1016/j.optcom.2014.01.037.

[79] E. D. Palik, Handbook of optical constants of solids, 2012. doi:10.1016/C2009-0-20920-2.

[80] D. P, CRC Handbook of Chemistry and Physics, Journal of Molecular Structure (1992). doi:10.1016/0022-2860(92)85083-s.

[81] R. Fuchs, Theory of the optical properties of ionic crystal cubes, Physical Review B (1975). doi:10.1103/PhysRevB.11.1732.

[82] D. STEELE, Chapter 7 - the later b-subgroup metals: Cu, ag, au; zn, cd, hg; (ga, in, ti); (ge), sn, pb; (as), sb, bi, in: D. STEELE (Ed.), The Chemistry of the Metallic Elements, The Commonwealth and International Library: Intermediate Chemistry Division, Pergamon, 1966, pp. 65 – 83. doi:https://doi.org/10.1016/B978-0-08-011853-6.50013-8.
URL http://www.sciencedirect.com/science/article/pii/B9780080118536500138

[83] X. López-Lozano, H. Barron, C. Mottet, H. C. Weissker, Aspect-ratio- and size-dependent emergence of the surface-plasmon resonance in gold nanorods-an ab initio TDDFT study, Physical Chemistry Chemical Physics (2014). doi:10.1039/c3cp53702a.

[84] E. Cottancin, G. Celep, J. Lermé, M. Pellarin, J. R. Huntzinger, J. L. Vialle, M. Broyer, Optical properties of noble metal clusters as a function of the size: Comparison between experiments and a semi-quantal theory, Theoretical Chemistry Accounts (2006). doi:10.1007/s00214-006-0089-1.

[85] D. Errandonea, The melting curve of ten metals up to 12 GPa and 1600 K, Journal of Applied Physics (2010). doi:10.1063/1.3468149.

[86] J. W. Goodman, Introduction to Fourier Optics Ch.4 2nd edition, Book (1996).

[87] D. Lin, P. Fan, E. Hasman, M. L. Brongersma, Dielectric gradient metasurface optical elements, Science (2014). doi:10.1126/science.1253213.

[88] J. Park, B. G. Jeong, S. I. Kim, D. Lee, J. Kim, C. Shin, C. B. Lee, T. Otsuka, J. Kyoung, S. Kim, K. Y. Yang, Y. Y. Park, J. Lee, I. Hwang, J. Jang, S. H. Song, M. L. Brongersma, K. Ha, S. W. Hwang, H. Choo, B. L. Choi, All-solid-state spatial light modulator with independent phase and amplitude control for three-dimensional LiDAR applications, Nature Nanotechnology (2020). doi:10.1038/s41565-020-00787-y.

[89] J. Zhang, M. ElKabbash, R. Wei, S. C. Singh, B. Lam, C. Guo, Plasmonic metasurfaces with 42.3% transmission efficiency in the visible, Light: Science and Applications (2019). doi:10.1038/s41377-019-0164-8.

[90] G. Kafaie Shirmanesh, R. Sokhoyan, R. A. Pala, H. A. Atwater, Dual-Gated Active Metasurface at 1550 nm with Wide (>300°) Phase Tunability, Nano Letters (2018). doi:10.1021/acs.nanolett.8b00351.

[91] M. L. Lin, J. M. Huang, C. S. Ku, C. M. Lin, H. Y. Lee, J. Y. Juang, High mobility transparent conductive Al-doped ZnO thin films by atomic layer deposition, Journal of Alloys and Compounds (2017). doi:10.1016/j.jallcom.2017.08.207.

[92] D. Dunmur, G. Luckhurst, Liquid Crystals, in: Springer Handbooks, 2007. doi:10.1007/978-0-387-29185-7_38.

[93] R. Deshpande, V. A. Zenin, F. Ding, N. A. Mortensen, S. I. Bozhevolnyi, Direct Characterization of Near-Field Coupling in Gap Plasmon-Based Metasurfaces, Nano Letters (2018). doi:10.1021/acs.nanolett.8b02393.

[94] W. T. Liu, J. Cao, W. Fan, Z. Hao, M. C. Martin, Y. R. Shen, J. Wu, F. Wang, Intrinsic optical properties of vanadium dioxide near the insulator-metal transition, Nano Letters (2011). doi:10.1021/nl1032205.

[95] M. M. Qazilbash, M. Brehm, B. G. Chae, P. C. Ho, G. O. Andreev, B. J. Kim, S. J. Yun, A. V. Balatsky, M. B. Maple, F. Keilmann, H. T. Kim, D. N. Basov, Mott transition in VO2 revealed by infrared spectroscopy and nano-imaging, Science (2007). doi:10.1126/science.1150124.

[96] I. Webman, J. Jortner, M. H. Cohen, Theory of optical and microwave properties of microscopically inhomogeneous materials, Physical Review B (1977). doi:10.1103/PhysRevB.15.5712.

[97] M. J. Dicken, K. Aydin, I. M. Pryce, L. A. Sweatlock, E. M. Boyd, S. Walavalkar, J. Ma, H. A. Atwater, Frequency tunable near-infrared metamaterials based on VO_2 phase transition, Optics Express (2009). doi:10.1364/oe.17.018330.

[98] E. Talebian, M. Talebian, A general review on the derivation of Clausius-Mossotti relation, Optik (2013). doi:10.1016/j.ijleo.2012.06.090.

[99] M. M. Qazilbash, A. Tripathi, A. A. Schafgans, B. J. Kim, H. T. Kim, Z. Cai, M. V. Holt, J. M. Maser, F. Keilmann, O. G. Shpyrko, D. N. Basov, Nanoscale imaging of the electronic and structural transitions in vanadium dioxide, Physical Review B - Condensed Matter and Materials Physics (2011). doi:10.1103/PhysRevB.83.165108.

[100] B. Liu, K. Song, J. Xiao, Two-Dimensional Optical Metasurfaces: From Plasmons to Dielectrics (2019). doi:10.1155/2019/2329168.